Safe Flutter Determination for Wings Undergoing Large Deflections

de Boer, S.; Karpel, M.; Sodja, J.

DOI
10.2514/6.2023-0379

Publication date
2023

Document Version
Final published version

Published in
AIAA SciTech Forum 2023

AIAA SciTech Forum
23-27 January 2023, National Harbor, MD & Online
AIAA SCITECH 2023 Forum

10.2514/6.2023-0379

Safe Flutter Determination for Wings Undergoing Large Deflections

Stefan de Boer*
Faculty of Aerospace Engineering, Delft University of Technology, 2629HS Delft, The Netherlands

Moti Karpel†
Technion—Israel Institute of Technology, 32000 Haifa, Israel

Jurij Sodja‡
Faculty of Aerospace Engineering, Delft University of Technology, 2629HS Delft, The Netherlands

A new flutter test version of the Parametric Flutter Margin (PFM) method, specifically applied to wings undergoing large deflections is presented. The PFM method adds a stabilising parameter, such as a stabilising mass, to the model such that the flutter velocity is increased. By exciting the stabilising mass in one of the primary (i.e., x, y and z) directions while simultaneously measuring the response in these directions and repeating the excitation in other directions, the flutter margins that are associated with the original model can be determined. To demonstrate the method a wind tunnel test campaign was performed at TU Delft using the Delft Pazy Wing which can exhibit large nonlinear deflection, onto which a flutter pod consisting of a shaker and stabilising mass was placed at the mid-span position at the leading edge of the wing. During the test campaign, three test series were performed. The first identified the flutter boundary through direct flutter tests, with the flutter onset and offset velocities being determined by actually hitting flutter that turned into an LCO. SISO and MIMO PFM tests were then performed to obtain the nominal flutter boundaries without actually hitting flutter, showing a maximum difference of 4.4 % between each other at an angle of attack of 6°. The difference between the MIMO and SISO PFM was found to be increasing with increasing angle of attack, which was as expected. Compared to the directly measured flutter tests, the MIMO PFM results identified a flutter velocity of 4.8 % lower than the directly measured flutter offset velocity at an angle of attack of 4°, and the SISO PFM results identified the flutter velocity to be 8.2 % lower than the offset velocity at 4° angle of attack. The PFM-identified flutter frequencies showed a difference of less than 2 % compared to the direct flutter test, with the difference in identified flutter frequency between the SISO and MIMO PFM reaching a maximum of 2 %. The acquired data shows the potential of the PFM method for performing safer, shorter and consequently cheaper flight tests for the certification procedure of new aircraft configurations.

Nomenclature

Abbreviations

MAC_{ODS}	Modal Assurance Criterion of the Operational Deflected Shape
AoA	Angle of Attack
ARMA	Autoregressive Moving Average
DOF	Degree of Freedom
FM	Flutter Margin
FRF	Frequency Response Function
GVT	Ground Vibration Test
LCO	Limit Cycle Oscillation
LE	Leading Edge
MAC	Modal Assurance Criterion
MIMO	Multiple-Input Multiple-Output
PCO	Phase Cross-Over
PFM	Parametric Flutter Margin
SISO	Single-Input Single-Output
TE	Trailing Edge

Symbols

*MSc Student, Faculty of Aerospace Engineering; s.deboer-2@student.tudelft.nl.
†Professor Emeritus, Faculty of Aerospace Engineering; karpel@technion.ac.il. Fellow AIAA.
‡Assistant Professor, Aerospace Structures and Materials Department; j.sodja@tudelft.nl. Senior AIAA member

α Angle of attack
Δp_f Stabilising mass needed to bring Nominal Configuration to Flutter Boundary, g
λ Eigenvalue
λ_f Eigenvalue at flutter boundary
$[A(i\omega)]$ Aeroelastic system matrix
$\left[B_f\right]$ Flutter margin input distribution matrix
$\left[C_f(i\omega)\right]$ Flutter margin output distribution matrix
$[T\,(i\omega)]$ Parametric flutter margin multiple-input/multiple output matrix
$\left\{B_f\right\}$ Flutter margin input distribution vector
$\left\{C_f(i\omega)\right\}$ Flutter margin output distribution vector
$\{x(i\omega)\}$ Vector of DOFs
μ Stabilising to moving mass ratio
ω Frequency, Hz
ω_{pco} Phase crossover frequency, Hz
ω_f Flutter/Limit-cycle oscillation frequency, Hz
$\Phi(i\omega)$ Phase, deg
$a_{mv}, \{a_{mv}\}$ Acceleration of shaking mass, m/s^2
$a_{st}, \{a_{st}\}$ Acceleration (Stabilising) stationary mass, m/s^2
$a_{s,c}$ Averaged moving mass acceleration
F Force, N
f Frequency, Hz
F_{ip} Averaged impedance head force
F_{ij} Force correction factor
g Damping
$G(i\omega)$ Gain
m_{mv} Mass of shaking mass, kg
m_{st} Mass of (Stabilising) stationary mass, kg
P_f Stabilising parameter
p_f Stabilising mass, g
Q_{ij} Mass corrected acceleration transfer function
S Span, m
$T\,(i\omega)$ Parametric flutter margin transfer function
T_{ij} PFM transfer function
U Velocity, m/s
$u_f, \left\{u_f\right\}$ Excitation input
$y_f, \left\{y_f\right\}$ Response stabilising parameter

I. Introduction

As part of the certification procedure, flight testing which proves that the flight envelope of the aircraft is flutter free is fraught with risk [1, 2]. During the flight tests, the flutter boundary is carefully approached up until the point that the damping coefficient reaches the 3 % threshold or that the flight envelope boundary is reached [3]. However, it is in some cases possible for the damping to decrease rapidly, which can lead to a sudden explosive flutter. Therefore, numerous numerical analyses, wind tunnel and ground tests are performed to make sure that the test aircraft is not accidentally brought too close to the flutter boundary. To be able to predict the flutter boundary during flight tests, several different data-analysis methods exist, such as the Zimmerman-Weissenburger flutter margin [4], damping extrapolation [5], the envelope function [6] and the Autoregressive Moving Average (ARMA) method [7]. All of these methods use the data obtained at velocities below the flutter speed to extrapolate the flutter boundary, which in turn leads to long, risky and expensive tests [8].

On the contrary, the numerical Parametric Flutter Margin (PFM) method developed by Roizner and Karpel [9, 10] formed a basis for an experimental method that safely determines the flutter condition by stabilising the system and analysing the frequency response functions (FRFs) of the stabilising element with respect to a co-located excitation force. A flutter margin (FM) with respect to the stabilising parameter is determined, based on which the flutter velocity can be determined through interpolation.

Two versions of the PFM method exist, single-input single-output (SISO) PFM and multiple-input multiple-output (MIMO) PFM. SISO PFM looks at the variation of the flutter characteristics with respect to a single stabilising parameter P_f [10], with a constraint of SISO PFM being that the effects of P_f can be formulated as a SISO feedback loop, leading to an incremental system matrix of rank-1, which means that the effect of P_f can only be analysed in a single direction whilst ignoring coupling effects. The MIMO PFM method removes the SISO PFM constraint by expanding the SISO open-loop equation of motion to include MIMO feedback, allowing for the representation of the effect of the stabilising parameter in an incremental system matrix of any rank [11].

The PFM method has been demonstrated on aeroelastic systems both numerically and experimentally. The numerical results obtained using the PFM method were compared to the results obtained using the MSC Nastran p-k and ZAERO g methods. The results showed that the SISO PFM results were practically identical to the conventional flutter determination methods for linear aeroelastic systems. The non-linear numerical flutter results showed that the LCO amplitudes calculated using the SISO PFM method are up to 7 % larger, however, this was considered acceptable for design studies [9, 10].

The first experimental application of PFM was performed by Sodja et al. on a 2 degree-of-freedom (DOF) typical section [8], who showed that the experimental and numerical SISO PFM method has very good to excellent agreement with the direct flutter test, as differences varying from 1 % to 6 % were found. Roizner et al. applied PFM to a flexible cantilever wing with an integrated stabilising mass [12]. The results showed that the differences in the flutter

velocity between the experimental PFM and numerical methods were less than 1 % and that the flutter modes and frequencies found using the PFM method were comparable with the numerical methods used in industry. The most recent experimental application of the PFM method to an aeroelastic system was performed by Karpel et al. [13]. The excitation device and stabilising parameter were integrated in this wind-tunnel experiment into a single flutter pod that consists of a shaker used to provide the excitation force, two accelerometers and a stabilising mass. The obtained result demonstrated a successful application of a shaker during the PFM tests, as a difference of 6.4 % with the numerical models was found. Since, as explained below, the PFM test positively indicates the nominal flutter boundary, the difference is more due to modelling errors than due to testing errors.

The PFM method has been applied numerically and experimentally to both linear and nonlinear aeroelastic systems. However, as an experimental flutter detection method, PFM has only been applied in its SISO form. With the shaker's mass used as a stabilizing parameter, the SISO approach is limited to cases where the effect of the added mass on flutter is significant only in one direction, normal to the lifting surface in the previously tested cases. The goal of this work is to apply MIMO PFM to a geometrically nonlinear aeroelastic system that is comprised of a highly flexible wing undergoing large aeroelastic deflections exhibiting operationally unacceptable LCOs beyond the flutter onset margin. With large deflections, the shaker's mass effects in the fore-and-aft direction become significant, which calls for the use of the MIMO approach.

The rest of this paper has the following structure. First, the PFM method is introduced in section II. This section presents the SISO PFM method as well as the extension to MIMO PFM. Secondly, the design of experiment is presented in section III, which is followed by section IV where the experimental procedures and different test setups used during the experiment are presented. The data analysis steps performed on the measured FRFs are shown in section V, and section VI present the obtained PFM results, as well as a comparison with the direct flutter tests and numerical simulations. Concluding remarks are given in section VII.

II. Parametric Flutter Margin Method

The formulation of the PFM method that has been implemented in this work for the identification of the flutter-onset boundary of a clamped highly flexible wing under large initial deflections is presented in this section. First, the SISO PFM method is presented in Section II.A, after which the modifications necessary to extend the PFM method to MIMO PFM are presented in Section II.B. Finally, Section II.C presents several methods available to excite the stabilising parameter and shows the selected excitation method.

A. SISO PFM

The formulation of the PFM method starts with the homogeneous aeroelastic equation given by

$$[A(i\omega)]\,\{x(i\omega)\} = \{0\} \tag{1}$$

To be able to apply the SISO-PFM method, the stabilising parameter, P_f, must be such that the incremental system matrix can be expressed as [9]

$$[\Delta A] = P_f \{B_f\} \left\{C_f(i\omega)\right\}^{\mathsf{T}} \tag{2}$$

with the constraint that the effect of the stabilising parameter can be removed using a SISO control feedback loop, leading to an incremental system matrix shown in equation (2) of rank-1. Because of this constraint, the effect of P_f can only be analysed in a single direction. Therefore, the augmented aeroelastic equation becomes

$$\begin{aligned} \left[A(i\omega) + P_f \left\{B_f\right\} \left\{C_f(i\omega)\right\}^{\mathsf{T}}\right] \{x(i\omega)\} &= \left\{B_f\right\} u_f(i\omega) \\ y_f(i\omega) &= \left\{C_f(i\omega)\right\}^{\mathsf{T}} \{x(i\omega)\} \end{aligned} \tag{3}$$

With the vectors $\left\{B_f\right\}$ and $\left\{C_f(i\omega)\right\}$ depending on the characteristics of the stabilising parameter, and u_f and y_f being the scalar input and output variables of the augmented aeroelastic equation. Using any $u_f(i\omega)$ that has a significant content over the frequency range of interest, equation (3) can be solved for $\{x(i\omega)\}$ and $y_f(i\omega)$.

At the flutter boundary, the input-output relation needs to satisfy

$$u_f(i\omega_f) = P_f y_f(i\omega_f) \tag{4}$$

such that the effect of P_f can be removed using a SISO feedback loop, with ω_f being the flutter frequency. Substituting equation (4) into equation (3), it can be shown that at the flutter boundary of the nominal system the effect of the stabilising parameter is removed by closing the SISO feedback loop, as the substitution removes the $P_f \left\{B_f\right\} \left\{C_f(i\omega)\right\}$ term which was added to form equation (3). Therefore, the flight conditions and excitation input that satisfy equation (4) indicate flutter. The resulting $\left\{x_f(i\omega)\right\}$ found using equation (3) is the flutter mode, as it is also a non-trivial solution to equation (1) [9, 10].

The conditions at which equation (4) is satisfied are determined by evaluating the following transfer function at different frequencies at selected velocities.

$$T\left(i\omega\right) = \frac{P_f y_f(i\omega)}{u_f(i\omega)} \tag{5}$$

Which can be expressed as gain and phase variations with frequency using the following equations [9, 10].

$$\begin{aligned} G\left(\omega\right) &= \left|\frac{P_f y_f(i\omega)}{u_f(i\omega)}\right| \\ \Phi\left(\omega\right) &= \angle\frac{P_f y_f(i\omega)}{u_f(i\omega)}\text{rad} \end{aligned} \tag{6}$$

Using the phase cross-over (PCO) frequencies (ω_{pco}), found at $\Phi\left(\omega_{\text{pco}}\right) = 0$, and the corresponding gain ($G\left(\omega_{\text{pco}}\right)$) the stability of the aeroelastic system can be determined. The nominal system will be stable, if $G\left(\omega_{\text{pco}}\right) < 1$, however, when $G\left(\omega_{\text{pco}}\right) > 1$ the nominal system will experience flutter [10]. Determining ω_{pco} and gain for multiple velocities, the point where $G\left(\omega_{\text{pco}}\right) = 1$, which is the flutter boundary, can be found. The corresponding ω_{pco} indicates the flutter frequency of the aeroelastic system.

B. MIMO PFM

As stated above, the SISO PFM method places a constraint on P_f that its effects can be removed using a SISO feedback loop, limiting the incremental system matrix to rank-1, which means that the effect of P_f can only be analysed in a single direction. In cases where the effect of P_f needs to be analysed in multiple directions, the rank-1 limitation of the representation of the stabilising parameter needs to be removed, with the removal of the rank-1 limitation leading to the MIMO PFM method.

A specific example of the requirement of the removal of the rank-1 limitation, is presented in this research as the modes that form the flutter mechanism will have a significant motion at the added mass point in both the normal and fore-and-aft directions (local z and x) with the local inertial effects in the spanwise and rotational directions still negligible, because of the large deflections experienced by the wing.

To be able to remove the rank-1 limitation, the SISO PFM method shown in equation (3) needs to be adapted to allow for a MIMO stabilising parameter. Following the steps presented in [11], the SISO PFM equation, shown in equation (3), is adapted to the following MIMO form.

$$\begin{aligned} \left[A(i\omega) + P_f \left[B_f\right] \left[C_f(i\omega)\right]\right] \left\{x(i\omega)\right\} &= \left[B_f\right] \left\{u_f(i\omega)\right\} \\ \left\{y_f(i\omega)\right\} &= \left[C_f(i\omega)\right] \left\{x(i\omega)\right\} \end{aligned} \tag{7}$$

Where $\left\{u_f\right\}$ and $\left\{y_f\right\}$ are now the input and output vectors, the $\left[B_f\right]$ and $\left[C_f(i\omega)\right]$ matrices are now able to be of any rank, up to the smaller number of variables in $\left\{y_f\right\}$ or $\left\{u_f\right\}$, leading to the ability to rewrite equation (7) to

$$\left\{y_f\right\} = \left[T(i\omega)\right] \left\{u_f\right\} \tag{8}$$

with $\left[T(i\omega)\right] = \left[C_f(i\omega)\right] \left[A\left(i\omega, U\right) + P_f \left[B_f(i\omega)\right] \left[C_f(i\omega)\right]\right]^{-1} \left[B_f(i\omega)\right]$ being the transfer function matrix. At the flutter boundary, the input-output relation now needs to satisfy

$$\left\{u_f(i\omega)\right\} = P_f \left\{y_f(i\omega)\right\} \tag{9}$$

Substituting equation (9) into equation (8) and replacing the real-valued P_f used in the right side of equation (9) with the complex valued λ^{-1}, the following eigenvalue problem is created.

$$\left[T(i\omega)\right] \left\{u_f(i\omega)\right\} = \lambda \left\{u_f(i\omega)\right\} \tag{10}$$

Solving for the eigenvalues of equation (10) for every frequency and velocity, the flutter boundary can be found at the flight conditions for which the eigenvalue is real and satisfies [11]

$$\lambda_f = \frac{1}{P_f} \tag{11}$$

Using the eigenvalues and the known stabilising parameter, the transfer functions can be converted into gain and phase using the following equations [14].

$$\begin{aligned} G(\omega) &= \left| \frac{\lambda_i(i\omega)}{P_f} \right| \\ \Phi(\omega) &= \angle \frac{\lambda_i(i\omega)}{P_f} \text{rad} \end{aligned} \tag{12}$$

To be able to determine the flutter margin, the $[T(i\omega)]$ matrix needs to be created for every velocity and every frequency from the measured FRFs, and its creation requires multiple steps. By exciting the stabilising parameter in one of the primary (i.e., x, y or z) directions and measuring the response of the stabilising parameter in all these directions, one column of the $[T(i\omega)]$ matrix can be created.

After the $[T(i\omega)]$ matrix has been created, the eigenvalue λ in equation (10) needs to be found. The process of creating the $[T(i\omega)]$ matrix and finding the corresponding λ needs to be repeated for every measured frequency within a single velocity, and is repeated for every velocity. Using the λ's found for all velocities and frequencies, the interpolated λ which satisfies equation (11) and $\lambda \in \mathbb{R}$ needs to be found, which is the eigenvalue at the flutter boundary λ_f. The velocity corresponding to λ_f, therefore, indicates the flutter boundary, with the associated eigenvector being the flutter mode at the location of the stabilising parameter. Using the eigenvector $\{u_f\}$ at the flutter velocity and flutter frequency, and the numerically known matrices $[A(i\omega)]$, $[B_f]$ and $[C_f]$, equation (7) can be solved for $\{x(i\omega_f)\}$, which represent the full flutter mode of the aeroelastic system.

C. Excitation of the Stabilising Parameter

As part of the application of the PFM method, the aeroelastic system needs to be excited to be able to measure the FRFs and search for the flutter condition. The previous experiments used a mass as a stabilising parameter which was excited in different ways. The experiment performed by Sodja et al. [8] used a modal hammer to provide an impulsive force to the stabilising mass. The application of PFM on a cantilever wing by Roizner et al. [12] used a string with an external weight attached. The input was provided by cutting the string, and from the known mass of the external weight, the step input on the stabilising mass could be found. As has been shown by Karpel et al. [13], the use of a shaker allows for the creation of a self-contained system that can be used during flight tests. The shaker also allows for controlled excitation levels, which means that the same excitation can be applied during multiple tests.

For this experiment, the aeroelastic system is excited using a shaker, which requires a modification to the input and output vectors. The vectors can be derived from Newton's laws. The input force vector on the shaker's static mass that serves as the stabilizing parameter is

$$\{u_f(i\omega)\} = -m_{\text{mv}} \{a_{\text{mv}}(i\omega)\} \tag{13}$$

where m_{mv} is the shaker's moving mass, and $\{a_{\text{mv}}(i\omega)\}$ the corresponding acceleration vector. The acceleration response of the stabilising mass m_{st} is given by

$$P_f \{y_f(i\omega)\} = m_{\text{st}} \{a_{\text{st}}(i\omega)\} \tag{14}$$

leading to the following input-output relation that needs to be satisfied at the flutter boundary

$$-m_{\text{mv}} \{a_{\text{mv}}(i\omega)\} = m_{\text{st}} \{a_{\text{st}}(i\omega)\} \tag{15}$$

The moving mass acceleration $\{a_{\text{mv}}(i\omega)\}$ and the stabilising mass acceleration $\{a_{\text{st}}(i\omega)\}$ are determined using accelerometers placed on the moving mass m_{mv} and on the stabilising mass m_{st}. As both m_{mv} and m_{st} are known, and the accelerations are measured, the matrix $[T(i\omega)]$ can be created for every velocity.

III. Design of Experiment

The application of MIMO PFM to a nonlinear aeroelastic system requires several steps. As a first step, a numerical model used to determine the expected static deformations and flutter behaviour of the wing has been developed and is presented in Section III.A, with the model validation shown in Section III.B. Finally, the results of the sensitivity study are shown in Section III.C, which shows the stability regions of the different wing configurations.

A. Numerical Model

To design the PFM experiment the anticipated flutter mechanism is modelled such that the position and amount of stabilising mass can be determined. The modelling approach follows the method presented by Howcroft et al. [15], which utilised the linear static aeroelastic deformation solver (SOL 144) within NASTRAN to calculate the static aerodynamic loads on the structure. The aerodynamic loads are then applied to the structure, and a nonlinear static analysis (SOL 106) is performed on the original structure to determine the nonlinear static deflections. To converge to the correct static nonlinear aeroelastic solution, the method iterates between SOL 144 and SOL 106 until the static solution is converged.

The procedure to calculate the static aeroelastic deflection is shown in Figure 1. The procedure was implemented using Python and MSC Nastran, which uses the linear aeroelastic trim solver (SOL 144) to calculate the aerodynamic loads, which are used as an input to the nonlinear SOL 400 solver to calculate the nonlinear deflection of the wing model. The SOL 400 solver was used to account for the geometrically nonlinear effects due to large deflections. Using the deformed structure, the aerodynamic mesh and structural mesh of the trim analysis are updated, which leads to a new aerodynamic load distribution. To account for the effect of the deformation, the load distribution from the previous iterations is added as a follower force acting in the opposite direction to provide the necessary incremental loads. This procedure is performed iteratively until the convergence criterion has been reached. For the static nonlinear solution to reach the convergence criterion, the incremental displacement in the out-of-plane (z) and the spanwise (y) directions was required to be less than 1 %. Using the converged displacement, the deformed structure can be modelled, and the corresponding eigenmodes and eigenfrequencies can be determined, which serve as input to the linear flutter analysis (SOL 145) to assess the aeroelastic flutter boundary of the wing in the deformed configuration.

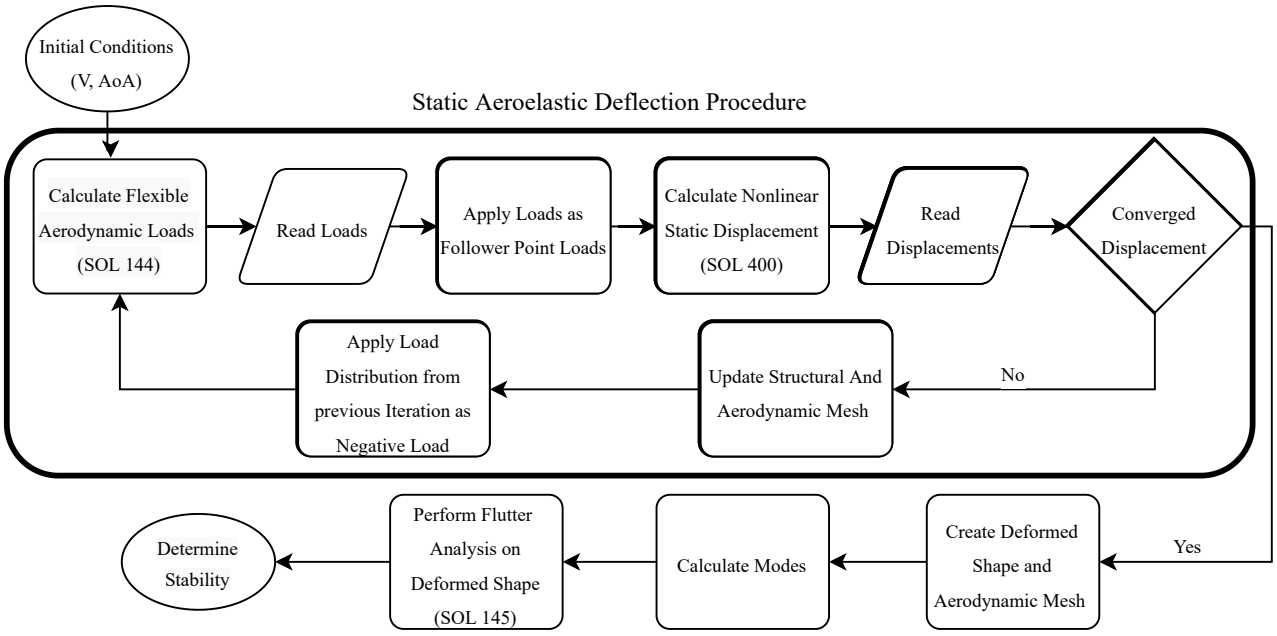

Fig. 1 Static aeroelastic deflection and flutter procedure

B. Model Validation

To validate the static nonlinear aeroelastic model and the modelled dynamic behaviour, the numerical results are compared to experimental deflection results and GVT results obtained by Mertens et al. [16],.

As a first step the static aeroelastic deflection is validated using the out-of-plane deflections of the Delft Pazy Wing at a free stream velocity of 18 m/s, and angles of attack $\alpha = 5°$ and $\alpha = 10°$ are compared. The comparison between the experimental results and the numerical results is shown in Figure 2. For the angle of attack, $\alpha = 5°$ the difference in tip displacement in the out-of-plane direction is over-predicted by 2.8 %. The tip displacement in the spanwise direction is under-predicted by 0.15 %. For $\alpha = 10°$ the difference in tip displacement is under-predicted by 1.5 % in the out-of-plane direction, and in the spanwise direction, the numerical displacement is equal to the experimentally determined displacement. Because of the small differences between the numerical model and the experimentally obtained deflections, the numerical model is validated to be in good agreement with the experimental results.

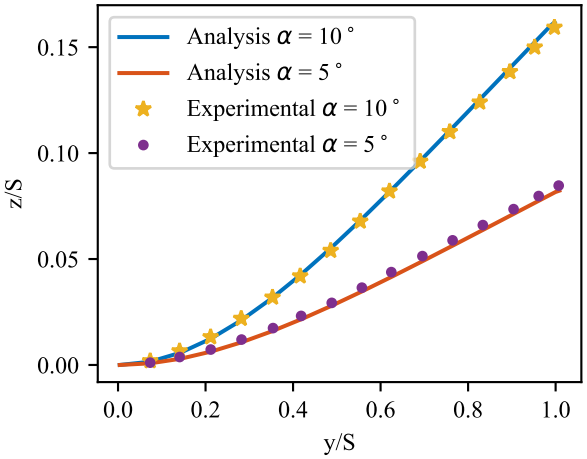

Fig. 2 Numerical model vs. experimental results. Experimental results obtained from Mertens et al. [16]

For the validation of the dynamic structural behaviour calculated using the presented numerical model, the GVT results obtained by Mertens et al [16] were used. The differences found for the out-of-plane modes were less than 4 %.

C. Flutter Results

The numerical stability region of the nominal configuration selected for the wind tunnel test campaign is shown in Figure 3. The first sensitivity study showed that the addition of small masses, in the order of 1 g to 2 g resulted in a different flutter behaviour in the order of 1 m/s to 3 m/s, hence, non-structural masses, such as the sensor cables and destabilising masses, were carefully included in the flutter analysis. The destabilising masses were necessary to bring the flutter velocity of the wing within the wind tunnel velocity range *. Looking at Figure 3 the expected flutter velocity at $\alpha = 0$ deg is at 25 m/s with the flutter velocity decreasing with increasing angle of attack. Looking at the corresponding Vg and Vf plots in Figures 4 – 7 for $\alpha = 0°$, 2°, 4° and 6° respectively, it can be seen that the first flutter mechanism is caused by the interaction between the 2nd Bending and 1st Torsion modes, while the second flutter region being caused by the 1st bending and 1st torsion interaction. These figures also show that the 2nd Bending – 1st Torsion flutter mechanism is a hump flutter mode that will stop when a sufficiently high velocity is reached. Looking at the evolution of the damping of the unstable mode in Figures 4 – 7, the reduction in flutter velocity and size of the hump mode with angle of attack are clearly shown.

Looking at the numerical flutter results for the PFM configuration, with 9.7 g added to the mid-span LE position, shown in Figure 3, it can be seen that the flutter velocity is drastically increased when compared to the nominal configuration. Therefore, it is possible to apply the PFM method to safely determine the flutter boundary of the nominal wing, over the entire range of angles of attack, without experiencing excessive vibrations.

Following the presented sensitivity study, three different wing configurations were designed and tested which are the

*https://www.tudelft.nl/lr/organisatie/afdelingen/aerodynamics-wind-energy-flight-performance-and-propulsion/facilities/low-speed-wind-tunnels/open-jet-facility [accessed 10 May 2022]

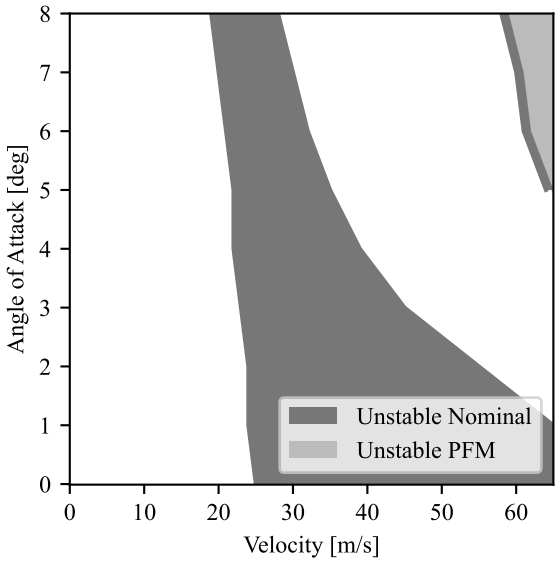

Fig. 3 Comparison stability region nominal and PFM configuration

Nominal, PFM and Full configurations respectively. The stability regions for the Nominal and PFM configurations have been discussed in this section. The Full configuration adds the moving mass of the shaker to the PFM configuration. To be able to distinguish between the different configurations, an overview of the components constituting the different configurations is shown in Table 1.

Table 1 Wing Configurations

Components	Nominal Configuration	PFM Configuration	Full Configuration
Shroud and Bolts	x	x	x
Sensor cables	x	x	x
Destabilising mass	x	x	x
Wing clamp and 3-axis accelerometer		x	x
Shaker stationary mass		x	x
Shaker moving mass			x

IV. Experimental Procedures

This section presents the different experimental setups and procedures used during the PFM wind tunnel test campaign.

A. Delft-Pazy Wing

The model used during the experimental test campaign is the Delft Pazy Wing. which was first used by Mertens et al. [16] and is based on the Pazy Wing designed at Technion and tested by Avin et al. [17]. The Delft Pazy Wing is a straight wing with a NACA0018 aerofoil and a 272 mm tip rod. The wing has a chord length of 100 mm and a span of 550 mm. The wing structure consists of a 3D-printed chassis made of Nylon 12 and an aluminium 7075 spar. The dimensions of the spar are 550 mm x 60 mm x 1.5 mm [16].

As part of the PFM wind tunnel test, several modifications were made to the Delft Pazy Wing. An overview of the added masses and sensors is shown in Figure 8. A 10 g mass (1) was placed on the tip rod, approximately 15 mm in

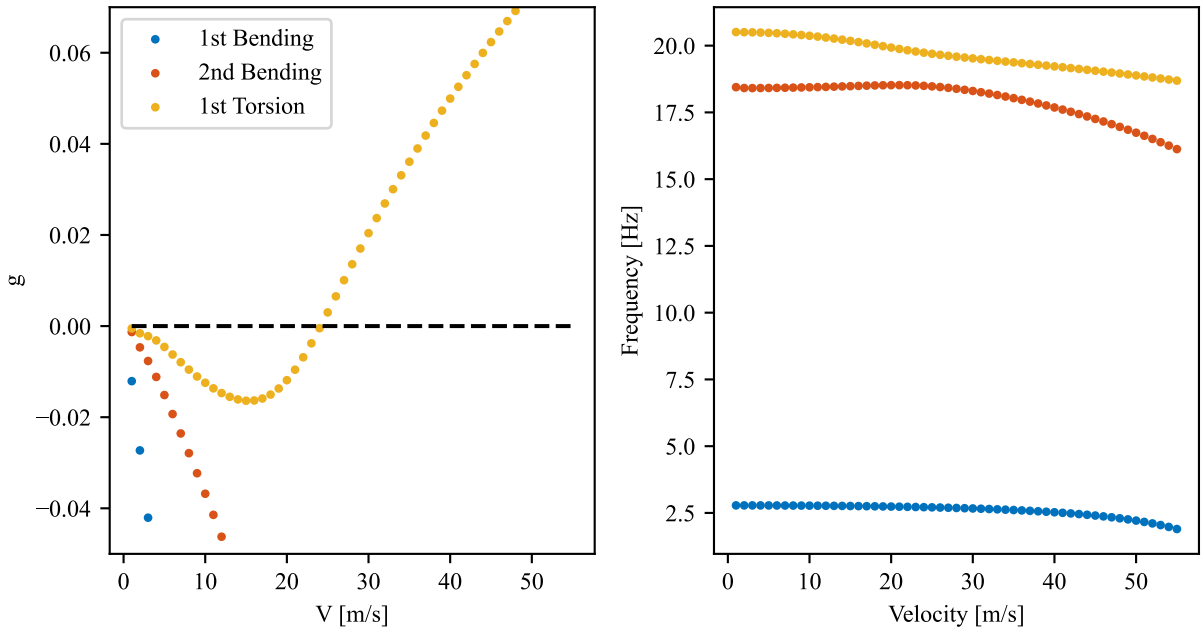

Fig. 4 Vg-Vf plot nominal configuration $\alpha = 0°$

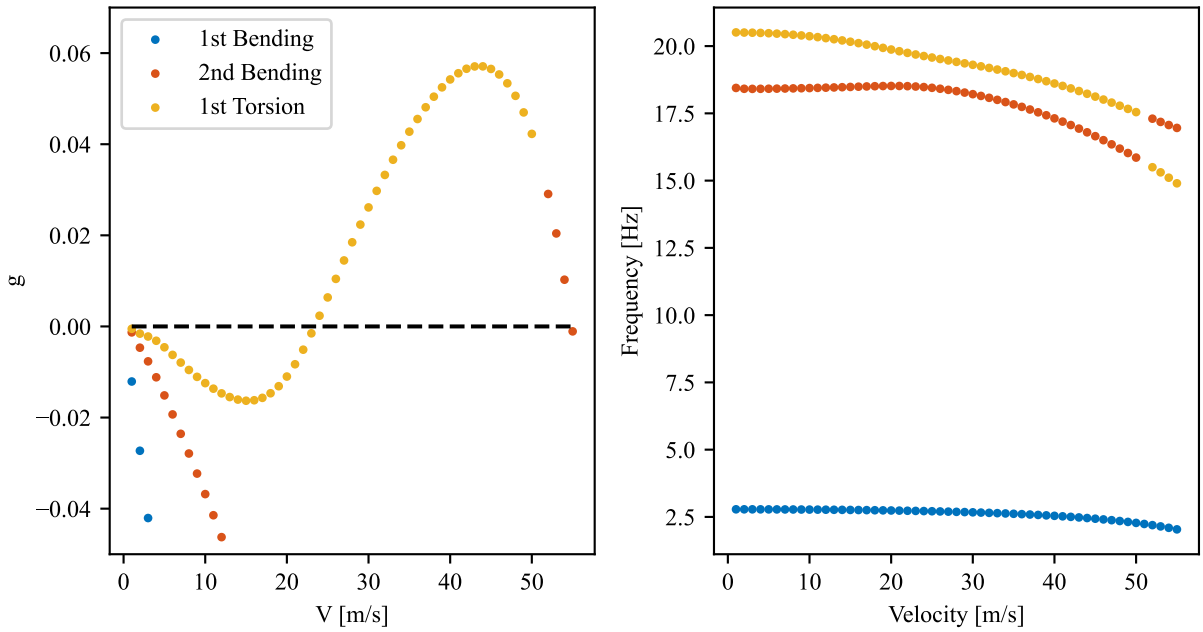

Fig. 5 Vg-Vf plot nominal configuration $\alpha = 2°$

front of the leading edge. Besides the 10 g mass at the leading edge (LE), a 3.2 g mass (2) was added to the rear of the tip rod. Both masses were added to reduce the flutter velocity of the 2nd Bending – 1st Torsion flutter mechanism to the tunnel's velocity range, by narrowing the gap between the two natural frequencies at low angles of attack.

Another modification made to the Delft Pazy Wing is the addition of several accelerometers. Eight 1-axis accelerometers (3) are embedded in the wing, and a tri-axis accelerometer (4) has been placed at the tip leading edge position. The accelerometers were placed to be able to monitor the system response during the test campaign.

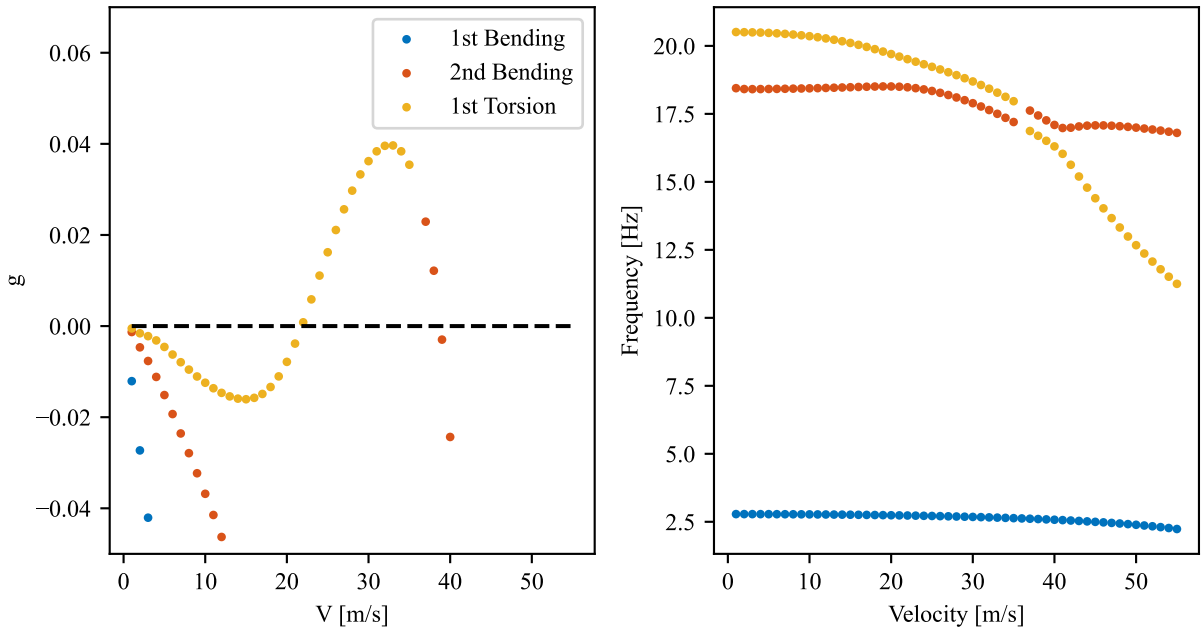

Fig. 6 Vg-Vf plot nominal configuration α = 4°

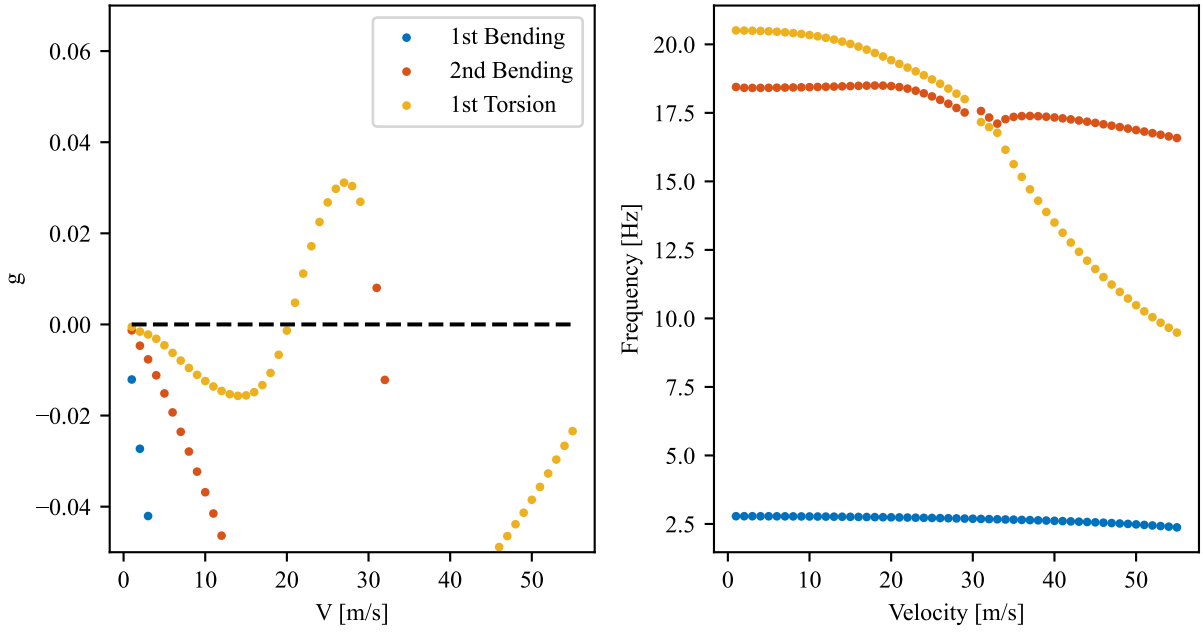

Fig. 7 Vg-Vf plot nominal configuration α = 6°

B. Parametric Flutter Margins Setup

To demonstrate the MIMO implementation of the PFM method, a flutter pod containing a micro-shaker system has been developed and integrated into the Delft Pazy Wing. The system consists of a shroud that is permanently attached to the wing, an electromagnetic shaker and the stabilising mass. The shroud (1) is shown in Figure 9, which also shows the stabilising mass (2) necessary for the PFM experiment. The stabilising mass consists of a 3D-printed wing clamp, which allows for the attachment of the shaker in the local x and z directions and a three-axis accelerometer used to measure the

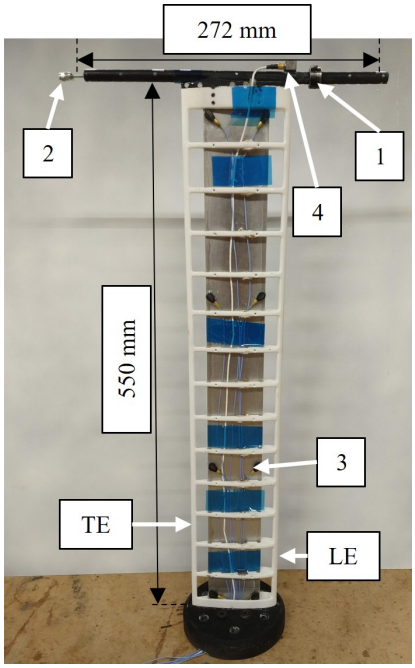

Fig. 8 Delft Pazy Wing with instrumentation. 1: 8x Single-axis accelerometer (PCB Piezotronics 352A24), 2: Destabilising mass 3.26 g, 3: Destabilising mass 10 g, 4: Tri-Axis Accelerometer (Dytran 3333A2T)

response of the stabilising mass, the shaker support, and the stationary voice coil of the shaker. The orientation of the tri-axis accelerometer on the stabilising mass is fixed throughout the tests, with the orientation of the shaker changing depending on the required excitation direction.

The electromagnetic shaker is shown in Figure 10 and consists of the moving and stationary components. The stationary components are the shaker's support (1) and stationary voice coil (2), which are part of the stabilising mass. The moving component of the shaker consists of a permanent magnet (3) and a single-axis accelerometer (4). The moving component of the shaker weighed 6.4 g, with all the stationary weight used to stabilise the system weighing 9.7 g. For both the PFM and Full configurations, the stabilising components and the shaker were placed in front of the leading edge at the mid-span position of the wing.

The system response and shaker excitation were measured and controlled using a Siemens Simcenter SCADAS Mobile Recorder [†], which measured the accelerations seen by the moving mass and stabilising mass from which the required FRFs were generated. The shaker was provided with a continuous random signal having a frequency content in the range between 1 and 30 Hz for a duration of 52 s per measurement. At every testing condition, the measurement was repeated three times to obtain an averaged FRF thereby increasing the signal-to-noise ratio.

C. Ground Vibration Tests

As part of the validation procedure of the numerical model, the modal behaviour of the model is investigated. To determine the difference between the numerical and experimental modal behaviour ground vibration tests (GVTs) were performed. An overview of the setup used during the GVTs is shown in Figure 11. The GVTs have been performed both in out-of-plane and in-plane directions to be able to capture the out-of-plane bending and torsion modes as well as the first lead-lag mode.

The GVTs were performed on two configurations called "Nominal" and "PFM". The nominal configuration which includes a shroud placed at the midspan position at the leading edge, all accelerometers embedded in the wing and the destabilising masses as presented in Figure 8, as well as the cables used for the accelerometers placed on the moving mass and stabilising mass. The PFM configuration adds the shaker and shaker attachment components that are part of the stabilising mass inside the mid-span shroud.

[†]Simcenter SCADAS Mobile and SCADAS Recorder, Siemens - Community support, 2022 `https://community.sw.siemens.com/s/article/simcenter-scadas-mobile-and-scadas-recorder` [accessed 9 October 2022]

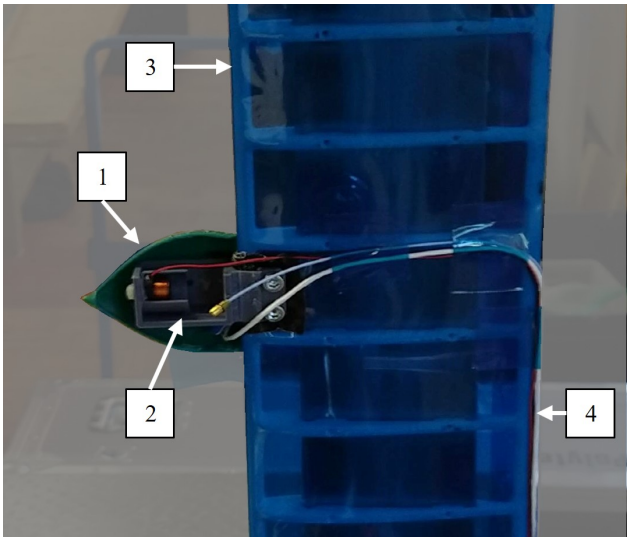

Fig. 9 Stabilising mass installed on delft pazy wing. 1: Delft pazy wing, 2: Shroud, 3: Stabilising mass, 4: Sensor cables (Part of Nominal Configuration)

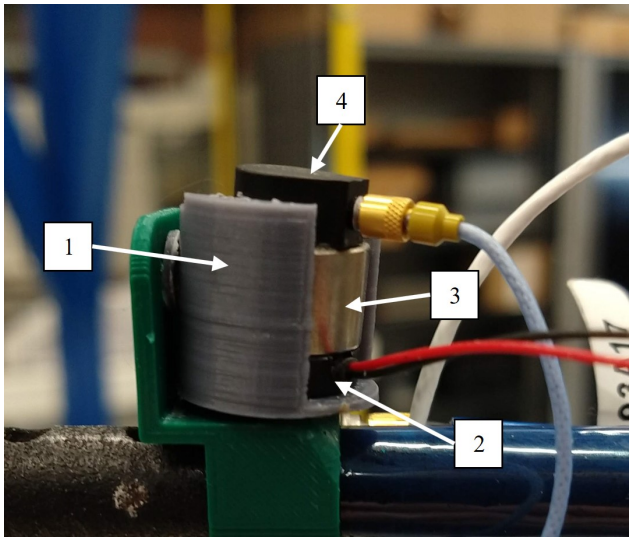

Fig. 10 Electromagnetic shaker. 1: Single-axis accelerometer (PCB Piezotronics 352A24), 2: Shaker support with end stops, 3: Moving permanent magnet, 4: Stationary voice coil

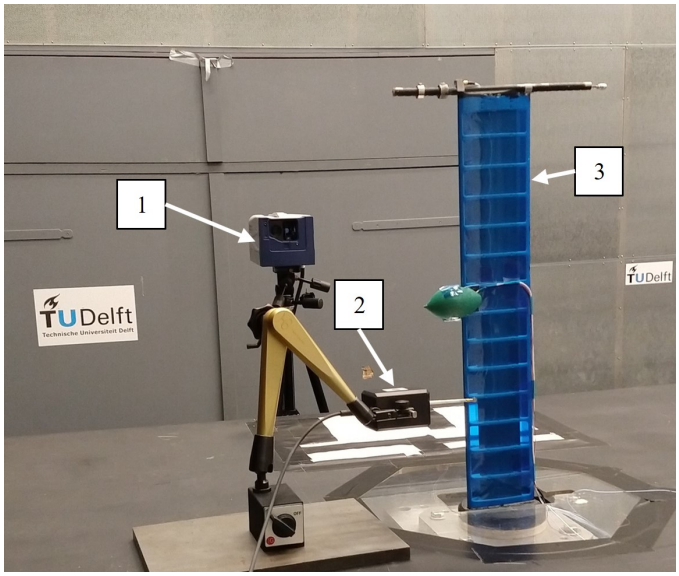

Fig. 11 Ground vibration test experimental setup 1: Laser scanning vibrometer, 2: Modal hammer, 3: Delft Pazy wing

The GVT measurements were performed using a Polytec PSV-500 laser scanning vibrometer (LSV) with a frequency range of up to 800 Hz, with the excitation of the wing being achieved using a Maul-Theet vImpact-61 automatic modal hammer [‡]. The LSV data has been processed using SimCenter TestLab. For the out-of-plane GVT, the vibration data was acquired at 24 points, as shown in Figure 12a. Nine measurement points were placed at the leading edge, nine at the trailing edge, six on the tip rod and one on the flutter pod. When running the GVTs on the configuration with the shroud at the midspan position, an extra measurement point was added to the shroud. For the in-plane GVT, the vibration data was measured at 8 points along the leading edge, and are indicated in Figure 12b.

[‡]Automatic Modal Hammer | vImpact vImpact-Serie `https://maul-theet.com/products/vibration-modal/hardware/automatic-modal-hammer/` [accessed 18 October 2022]

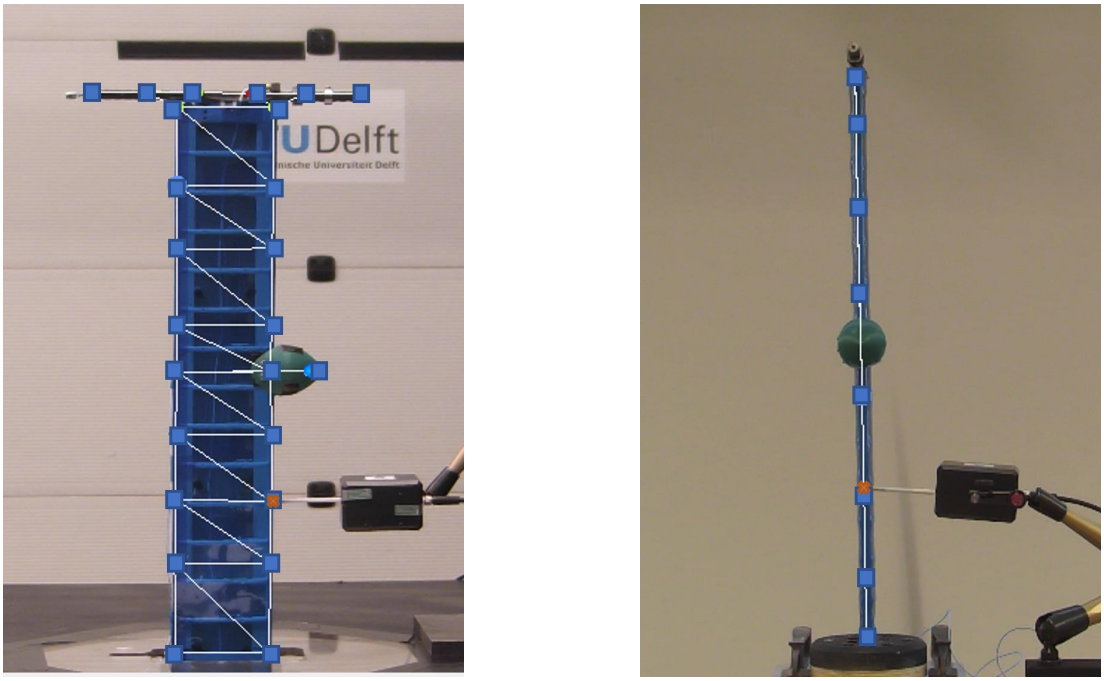

a) Out-of-plane **b) In-plane**

Fig. 12 GVT measurement points (blue squares) and the driving point (red cross)

The comparison between the GVT results obtained using the presented GVT setup and the analysis model is shown in Table 2. It is interesting to note that the out-of-plane and torsional modes are captured well, whereas the in-plane mode is not. The difference in the in-plane direction is most likely caused by the difference in the clamping of the main spar in the numerical model and the experiment, as the main spar is clamped using two aluminium blocks at its root which allows for more freedom of movement in the for-and-aft direction when compared to the numerical model. However, the large difference for the 1st In-Plane Bending mode does not cause a detrimental effect on the predicted flutter velocity because its natural frequency is still well above the 1st torsion frequency and the expected flutter frequency.

Table 2 Comparison between the analysis model and the GVT results

	Nominal Configuration			Full Configuration		
Mode Type	f_{FEM} [Hz]	f_{GVT} [Hz]	Δf [%]	f_{FEM} [Hz]	f_{GVT} [Hz]	Δf [%]
1st Bending	2.8	2.9	-3.1	2.7	2.8	-2.6
2nd Bending	18.5	19.6	-5.6	17.4	19.1	-8.6
1st Torsion	20.5	21.5	-4.4	20.3	20.5	-1.0
3th Bending	60.3	63.3	-4.79	60.2	62.5	-3.7
2nd Torsion	78.7	80.8	-2.6	72.3	70.2	2.9
1st In-Plane Bending	91.6	58.9	55.4	90.7	58.2	55.9

Using the GVTs performed on the final wing model, the numerical model was updated such that the flutter behaviour of the wind tunnel configuration could be determined. The stability region plots shown in section VI have been generated using the updated numerical model.

D. Wind Tunnel Setup

The PFM wind tunnel experiments were performed in the Open Jet Facility (OJF) at Delft University of Technology, which is a closed-loop wind tunnel with an open test section. The octagonal outlet of the OJF spans 2.85 m x 2.85 m and can reach a maximum velocity of 30 m/s *.

The wind tunnel setup and the relevant components are indicated in Figure 13, with Delft Pazy Wing model (1) attached vertically in the OJF test section and placed on a six-degree-of-freedom force balance (2) mounted to a rotating table (3) which allows for the setting of the geometric angle of attack, α, with respect to the inflow. To reduce the wind tunnel interference effects, the balance and rotating table were placed below a splitter plate (4). The SCADAS Mobile data recorder (5) and Power amplifier (6) indicated in Figure 13 are used to control and measure the flutter pod excitation and system response. To measure the wing deflection and the tip oscillation during the LCO, an OptiTrack [§] motion recovery system was used.

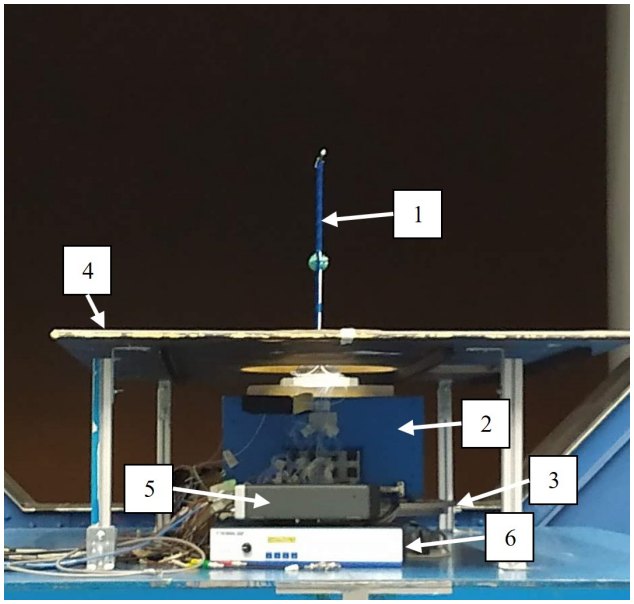

Fig. 13 Wind tunnel setup; Looking upstream. 1: Delft pazy wing, 2: 6-Component force balance, 3: Rotating table, 4: Splitter plate, 5: Siemens Simcenter SCADAS Mobile data recorder, 6: Power amplifier

V. Data Analysis

Within this section, the data analysis steps taken to evaluate the measured FRFs and obtain the corresponding flutter margins are presented. First, the data smoothing process is described, after which the required correction factors to account for are presented. Finally, the assembly process of the MIMO PFM transfer function matrix, $[T(i\omega)]$, is described.

A. Scaling

As a first step within the data analysis, the raw acceleration FRF must be scaled, with the ratio of stabilising and moving masses (μ), to get the FRFs required for PFM. The measured FRFs are in the form

$$Q_{ij} = \mu \frac{a_{\mathrm{st},i}}{a_{\mathrm{mv},j}} = \frac{m_{\mathrm{st}} a_{\mathrm{st},i}}{m_{\mathrm{mv}} a_{\mathrm{mv},j}} \quad i,j = x,z \tag{16}$$

After the mass fraction μ has been applied to the measured acceleration FRFs, the force correction factor can be applied to the FRF signal. The force correction factor is an FRF that relates the force measured using the single-axis accelerometer on the moving mass to the actual force generated by the shaker and is necessary because of the mounting

[§] OptiTrack `https://optitrack.com/` [accessed 25 October 2022]

of the single-axis accelerometer on the moving mass. The shaker force is measured by placing the shaker and its support on a PCB Piezotronics 288D01 Impedance Head [¶].

To capture the force over the whole measurement range, a sine-sweep was performed and the acceleration of the moving magnet was measured using the accelerometer. During testing, it was found that the tension on the accelerometer cable influenced the shaker's behaviour. Therefore measurements using the LSV were performed to characterise the effect of the accelerometer cable on the moving mass force. An overview of the setup used to determine the FRFs of the shaker force is shown in Figure 14.

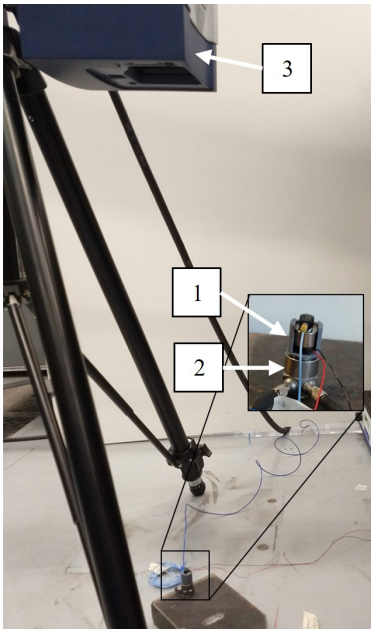

Fig. 14 Shaker Calibration Setup. 1: Shaker assembly, 2: Impedance Head (PCB Piezotronics 288D01), 3: Laser Scanning Vibrometer

The raw FRF measurements used to determine the correction factor are shown in Figure 15. Within the region of interest, 15 Hz to 30 Hz, indicated with the vertical lines, it can be seen that the effect of the cable on the shaker response is negligible, as the FRF responses with and without cable are equivalent. However, looking at both the acceleration measured using the LSV and the single-axis accelerometer, it can be concluded that the acceleration of the moving mass, and therefore the force, is underestimated assuming Newton's second law.

The force correction factor, F_{ij} is created by smoothing all measured FRFs using a gaussian filter, after which the smoothed shaker force responses are averaged to create a single complex and frequency-dependent correction factor F_{ij}, which is applied to the mass-corrected transfer function Q_{ij} to create

$$T_{ij} = Q_{ij} \cdot F_{ij} = \frac{m_{\text{st}} a_{\text{st},i}}{m_{\text{mv}} a_{\text{mv},j}} \cdot \frac{m_{s,\text{mv}} a_{s,c}}{F_{\text{ip}}} \quad i,j = x,z \tag{17}$$

which is a frequency-dependent complex value where F_{ip} is the average of all measured impedance head forces and $a_{s,c}$ is the averaged acceleration from all performed measurements.

B. Data Smoothing

To be able to use the measured FRFs in the transfer function matrix, $[T\,(i\omega)]$, a gaussian filter is applied directly to the complex FRF signal such that the noise in the signal is reduced, and the resulting complex number at each frequency can be used to create $[T\,(i\omega)]$. Examples of the performed smoothing are shown in Figure 16.

Specifically looking at the figures with the z-excitation, Figures 16a and 16b, it can be seen that the noise in the signal is minimal, which is supported by the high coherence values shown in Figure 17a. Figures 16c and 16d, which show

[¶]PCB Piezotronics Model: 288D01 | Mechanical Impedance Sensor `https://www.pcb.com/products?model=288d01` [accessed 12 October 2022]

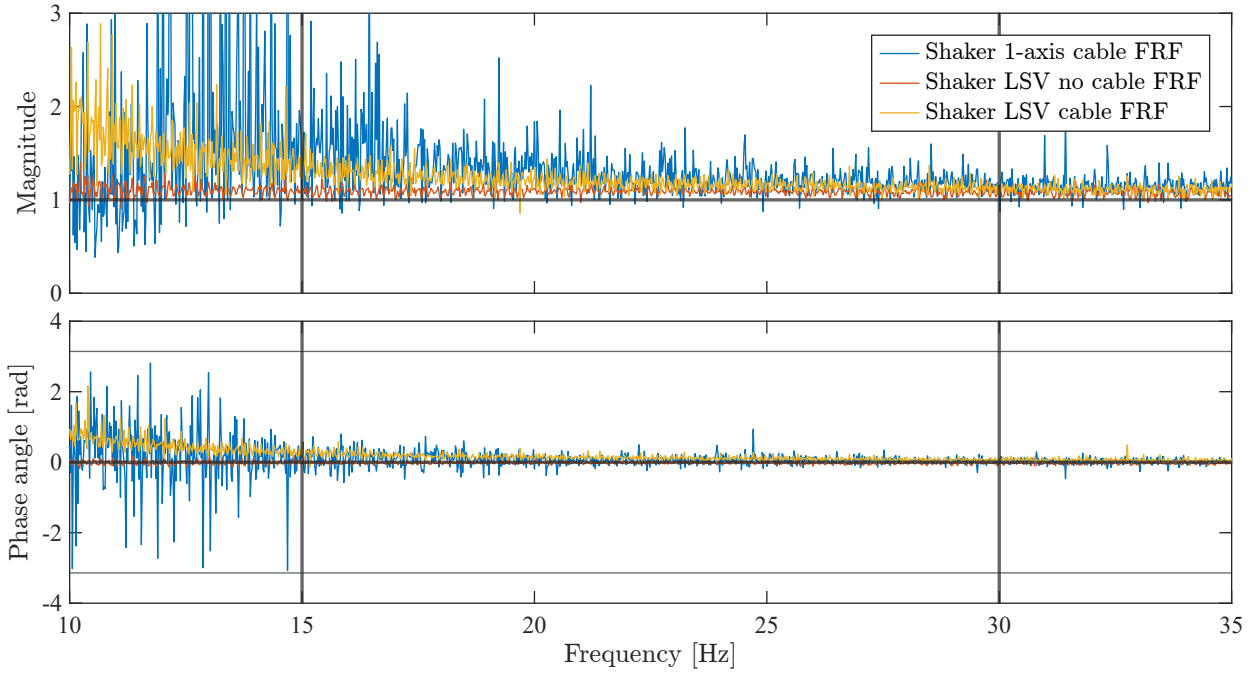

Fig. 15 Shaker Force FRF: $F_{\text{correction}}/F_{\text{impedance head}}$

the response FRFs corresponding to an x-excitation present a response with a lot of noise as is indicated with the low coherence values in Figure 17b. Because of the noisy response in the x-excitation signal, only the magnitude of these signals was smoothed, with the phase remaining as measured, such that the the effect of the PCOs, as seen in Figure 16c, can be captured, because the smoothing of the complex number resulted in a constant phase and under-valued magnitude that was not able to represent the behaviour of the measured FRF.

C. MIMO Parametric Flutter Margin

As stated in section II.B the transfer function matrix, $[T\,(i\omega)]$, needs to be created for every velocity and frequency and is assembled as follows

$$[T\,(i\omega)] = \begin{bmatrix} T_{xx}\,(i\omega) & T_{xz}\,(i\omega) \\ T_{zx}\,(i\omega) & T_{zz}\,(i\omega) \end{bmatrix} \tag{18}$$

The transfer function matrix only includes the response and excitation in the x- and z-direction. The y-contribution in the transfer function matrix can be disregarded because, in the experimental deflection range, the local spanwise motion of the wing at the shaker's location is not coupled with the fore-and-aft and out-of-plane motion and the local inertial effects of the stabilising parameter in the spanwise and rotational directions are negligible.

Solving for the eigenvalues of the 2x2 matrix $[T\,(i\omega)]$, two eigenvalues, λ_1 and λ_2 are found. Using the eigenvalues calculated at every frequency, the evolution of the eigenvalues with respect to the frequency can be determined. The eigenvalue evolution, for $\alpha = 0°$ and $2°$, of λ_1 is shown in Figure 18, and the evolution of λ_2 is shown in Figure 19. Figures 18 and 19 show the eigenvalue evolution for multiple velocities, with each velocity representing a different measurement. From the eigenvectors corresponding to λ_1 and λ_2 shown in Figure 20, it can be seen that λ_1 is dominated by the response in the x-direction and λ_2 by the response in the z-direction.

As can be seen in Figure 18, the λ_1 eigenvalues are very small, and far below a value that can satisfy equation (11), and are therefore discarded. The evolution of λ_2 shown in Figure 19 shows a clear path followed by the eigenvalues as well as a larger magnitude. Therefore the λ_2 evolution is used to determine the stability of the aeroelastic system.

The λ_2 evolution for $\alpha = 0°$ and $2°$ is shown in Figure 19. In general, three different types of eigenvalue evolutions can be found, which are an evolution with no PCO, an evolution with a PCO and an evolution with a phase flip (phase jumps from $+\pi$ to $-\pi$ or vice versa) and PCO occurring on the real and positive axis. An eigenvalue evolution experiencing a phase flip first crosses Im $(\lambda) = 0$ axis with the real component being smaller than zero. An example of

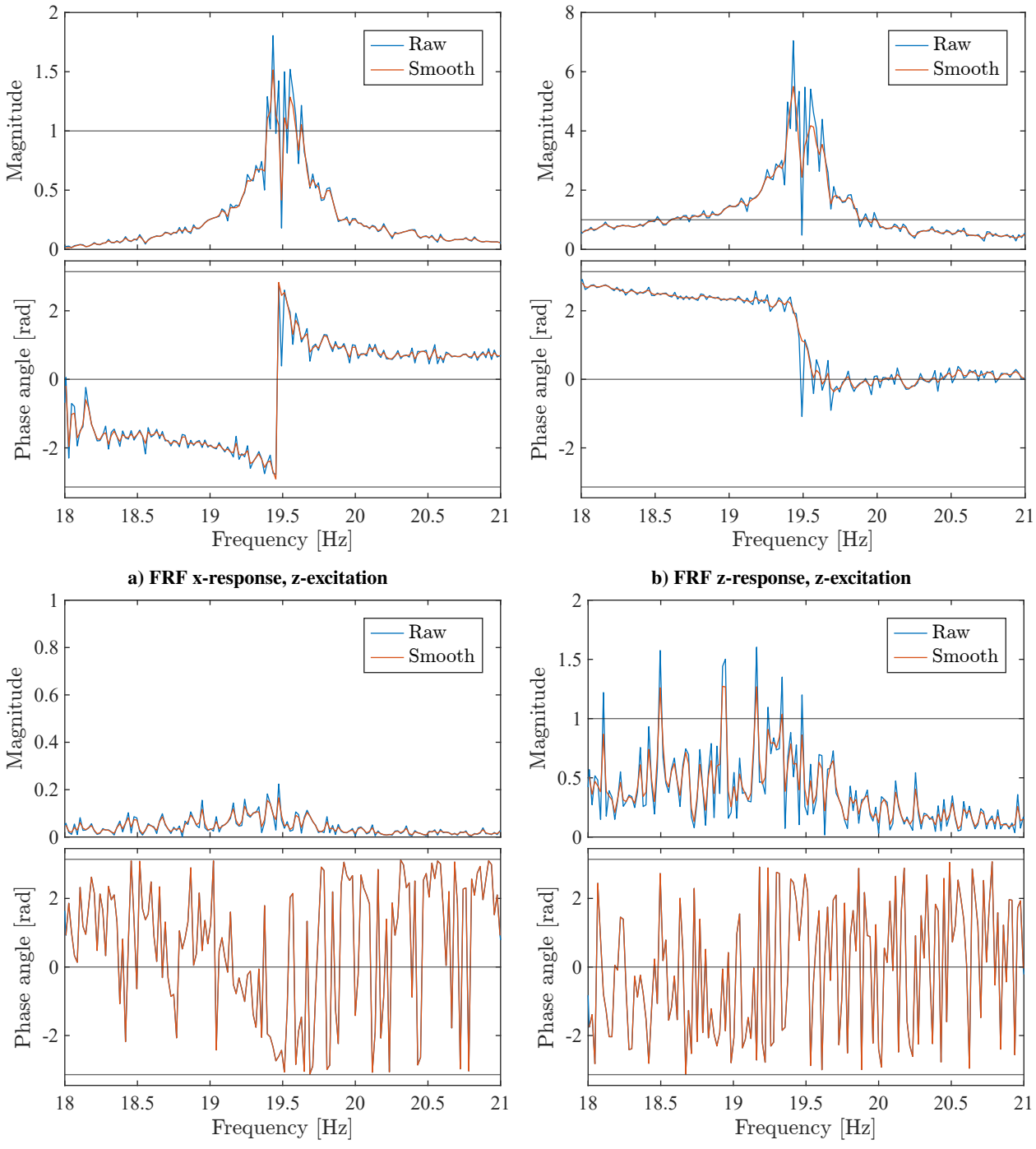

a) FRF x-response, z-excitation

b) FRF z-response, z-excitation

c) FRF x-response, x-excitation

d) FRF z-response, x-excitation

Fig. 16 FRFs $\alpha = 2°$, 21 m/s

which is shown in Figure 19 for $\alpha = 0°$ and $2°$ for 25 m/s and 20 m/s respectively. The eigenvalue evolution for $\alpha = 0°$ at 22 m/s shows a PCO with a gain greater than 1, with $\alpha = 2°$ at 20 m/s having a gain less than 1 and a gain greater than 1 for 21 m/s. Finally, 20 m/s for $\alpha = 0°$ shows an eigenvalue evolution that has no PCO, as it does not cross the $\mathrm{Im}(\lambda) = 0$ axis.

To determine the stability of the aeroelastic system, the $\lambda_2 \in \mathbb{R}$ and $\lambda_2 > 0$ are collected for each velocity, with the $\lambda_2 \in \mathbb{R}$ indicating a PCO. By collecting $|\lambda_2| = \lambda_f P_f$ for each velocity, the stability of the aeroelastic system

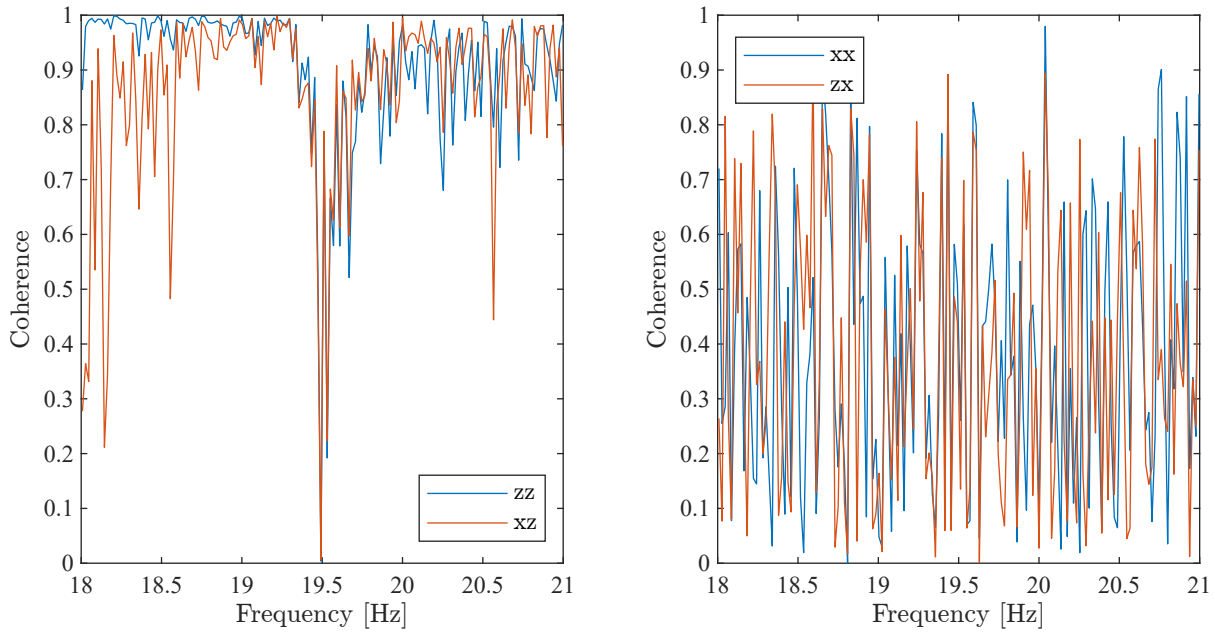

a) Coherence z-response, and x-response due to z-excitation **b) Coherence z-response, and x-response due to x-excitation**

Fig. 17 Coherence $\alpha = 2°$, 21 m/s

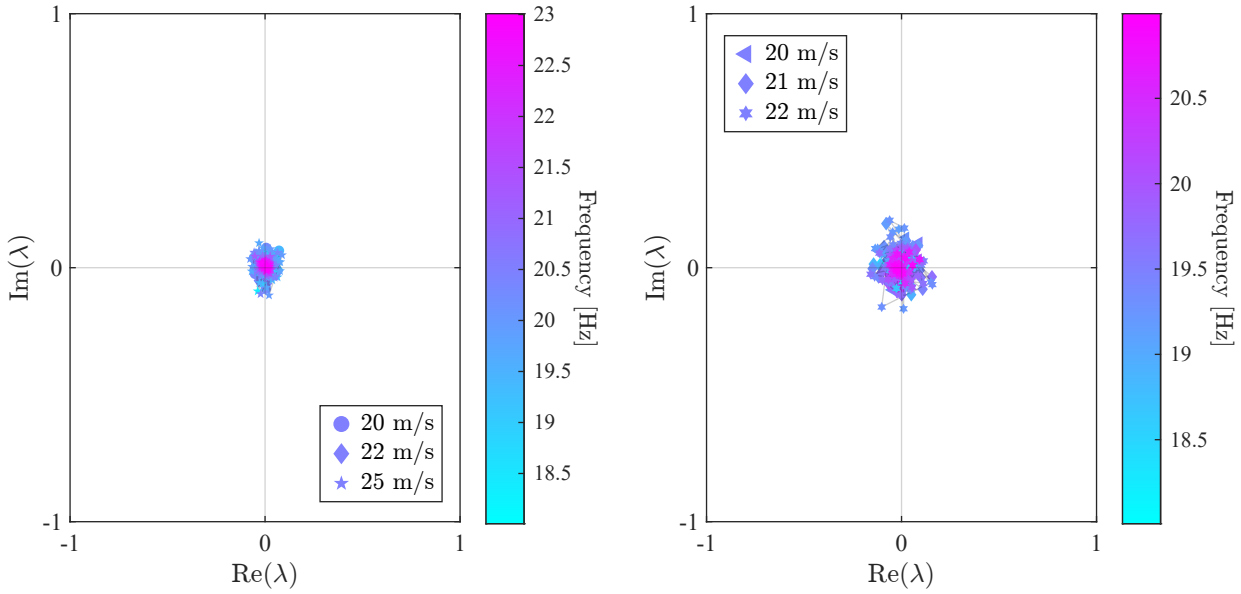

a) $\alpha = 0°$ **b) $\alpha = 2°$**

Fig. 18 λ_1 evolution

is determined, with $\lambda_f P_f < 1$ indicating a stable aeroelastic system at the corresponding velocity, and $\lambda_f P_f > 1$ indicating an unstable system. Using the collected $|\lambda_2|$, the velocity at which equation (11) is satisfied can be found.

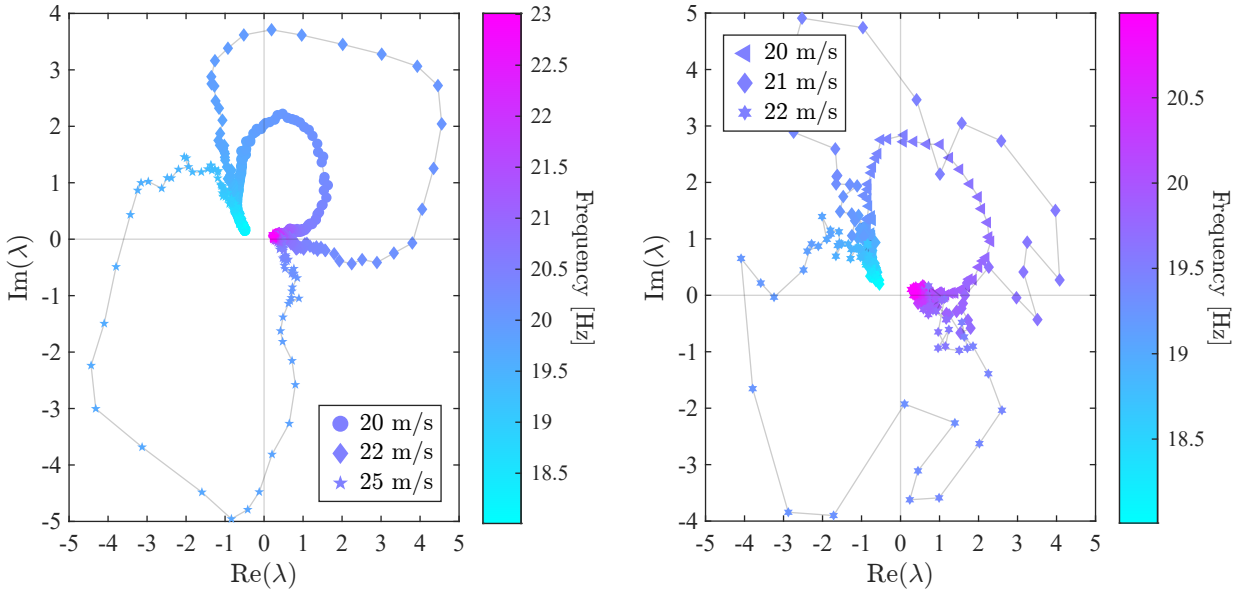

a) α = 0° **b) α = 2°**

Fig. 19 λ_2 evolution

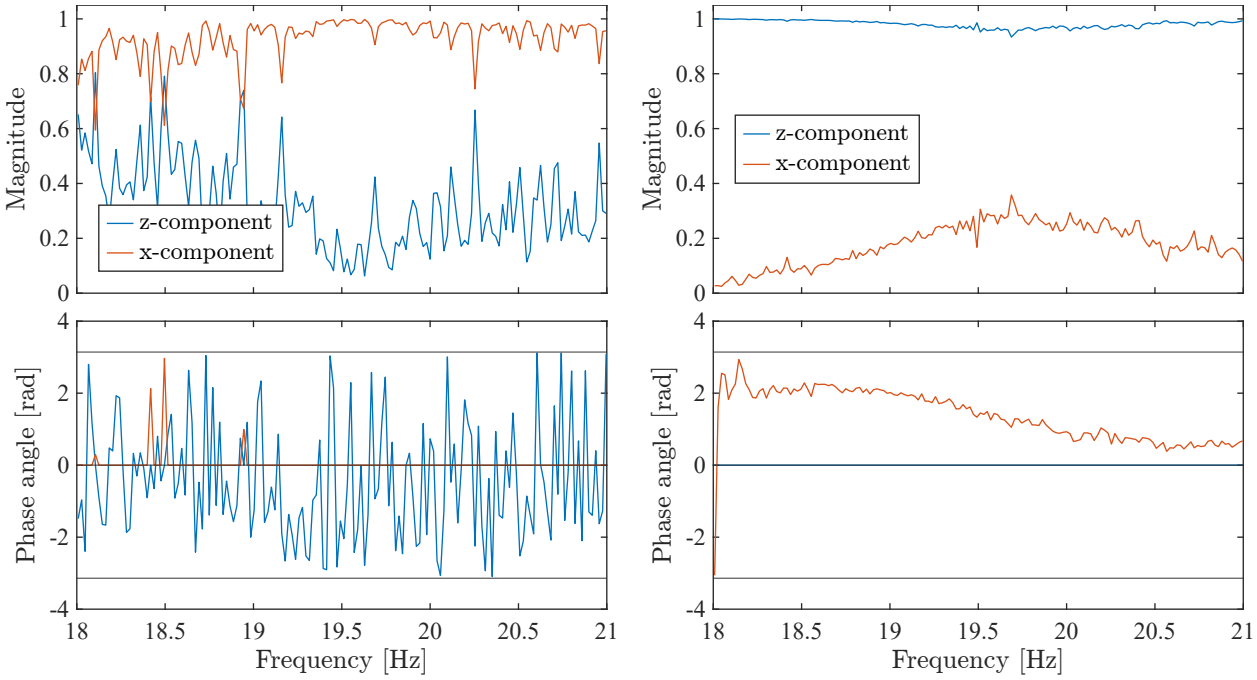

a) Eigenvector corresponding to λ_1 **b) Eigenvector corresponding to λ_2**

Fig. 20 Eigenvector α = 2°, 21 m/s

VI. Experimental Flutter Results

The results obtained during the wind tunnel test campaign are presented and discussed in this section. First, the flutter onset and offset velocities measured during the direct flutter tests are presented, followed by the PFM results, in which a comparison between the SISO and MIMO PFM results, direct flutter test and numerical results is presented. Finally, the effect of different shaker excitation levels is shown.

A. Direct Flutter Tests

A very significant advantage in performing flutter tests with a very flexible wing is that the flutter vibrations often turn into limit-cycle oscillations (LCO) without damaging the test model structure, as happened in the presented test and in Drachinsky et al. [18]. Therefore, to be able to correlate the PFM results to the actual flutter velocities of the wing, direct flutter tests have been performed with the nominal configuration for $\alpha = 0°, 2°, 4°$ and $6°$. Two direct flutter tests were performed for each angle of attack. In the first test, the wind tunnel velocity was slowly increased until the wing would start to flutter which was recorded as the flutter onset velocity. In the second test, the wind tunnel velocity was increased beyond the flutter onset velocity. The wing was allowed to settle on a stable LCO after which the wind tunnel velocity was gradually decreased until the LCO disappeared. This velocity was recorded as the flutter offset velocity. An overview of the obtained flutter onset and offset velocities are presented in Table 3. Direct flutter tests were also performed on the PFM configuration, and they exhibited no flutter over the entire wind-tunnel velocity range.

Interesting to note, is that the wing at $\alpha = 6°$ experienced no flutter within the wind tunnel velocity range, which can have several reasons. A reason could be the fact that because of the deflections experienced by the wing, which ranged from 64 mm (11.6 % of the span) at 16 m/s to 107 mm (19.5 % of the span) at 21 m/s. The deflection could have caused the 1st torsion mode and 2nd bending modes to flip and not allow the modes to couple enough with each other for flutter to occur, or because the actual structural damping coefficient was larger than the assumed coefficient.

Table 3 Direct flutter test results of the nominal configuration

α (°)	Onset (m/s)	Offset (m/s)	LCO frequency (Hz)
0	24.2	21.5	20.3
2	21.6	21	19.4
4	21	19.5	19.2
6	> 29	> 29	-

B. PFM Results

1. Gain and Phase Cross-Over Frequency

Using the data analysis steps described in section V, the phase cross-over frequency and corresponding gain at each velocity can be determined, which results in Figures 21 to 23 that show the SISO and MIMO PFM results for $\alpha = 0°, 2°$ and $4°$ respectively. The measurement results can be split into two different datasets, with the first dataset containing a phase cross-over and the second dataset containing phases of less than 10°, but no zero phase crossing, which is indicated using a dashed line. The vertical dashed lines are used to indicate the boundaries of the different datasets. The phase cross-over dataset contains two types of results, one where only a phase cross-over is found and one where both a phase flip and a phase cross-over on the positive real axis are present within the signal. Within the phase cross-over region, the gain is first increasing, and after a certain velocity, the magnitude drops below 1 again. The drop in gain is a characteristic of an eigenvalue evolution with a phase flip and PCO and is caused by the phase flip in the $T_{zz}(i\omega)$ FRF, which leads to a higher phase cross-over frequency.

The PFM results for $\alpha = 0°$ in Figure 21, show that the SISO and MIMO PFM methods provide the same gain and cross-over frequency results. This is expected, as $\alpha = 0°$ is the limit case with the wing experiencing no static deflections, and therefore, ano coupling between x and z directions is expected.

Looking at the PFM results for non-zero α, shown in Table 4, it can be seen that the MIMO and SISO PFM methods exhibit an increasing difference in the flutter velocity V_f, up to a maximum of 4.4 % for $\alpha = 6°$. The difference in PCO frequency, ω_{pco}, between MIMO and SISO is also increasing with increasing α, and it reaches a maximum of 2 % for

$\alpha = 6°$. In general, it can be stated that the MIMO PFM method provided a slightly higher flutter velocity, and lower PCO frequency.

Looking specifically at the PFM results for $\alpha = 6°$ in Figure 24, it can be seen that no direct flutter onset and offset velocities have been found, as indicated in the previous section. However, both the SISO and MIMO PFM results indicate that flutter is occurring around 19 m/s, with the numerical model predicting the flutter onset at 21 m/s. The identification of flutter using the PFM method, and not using direct flutter testing is most likely caused by the fact that the flutter mechanism is occurring within the aeroelastic system, however, the flow can not provide sufficient energy needed to start the flutter process, which often occurs with very moderate flutter mechanisms, leading to the detection of flutter using the PFM method but not through direct flutter testing.

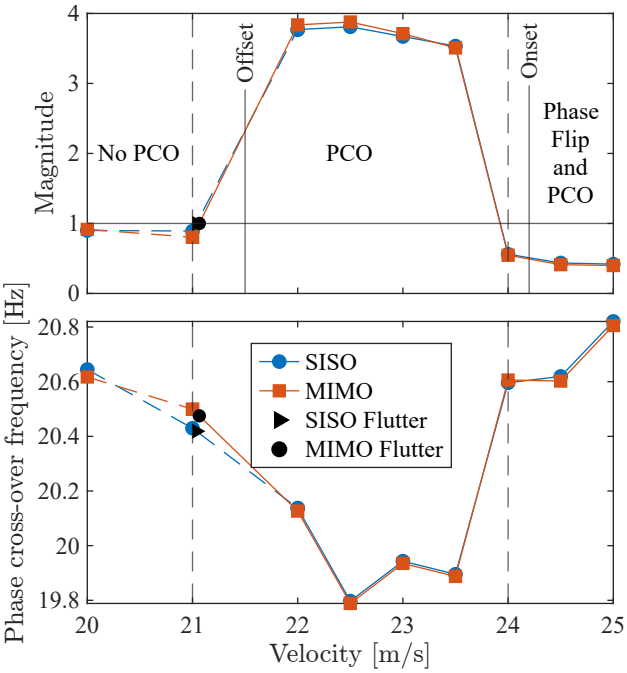

Fig. 21 Comparison SISO vs. MIMO $\alpha = 0°$

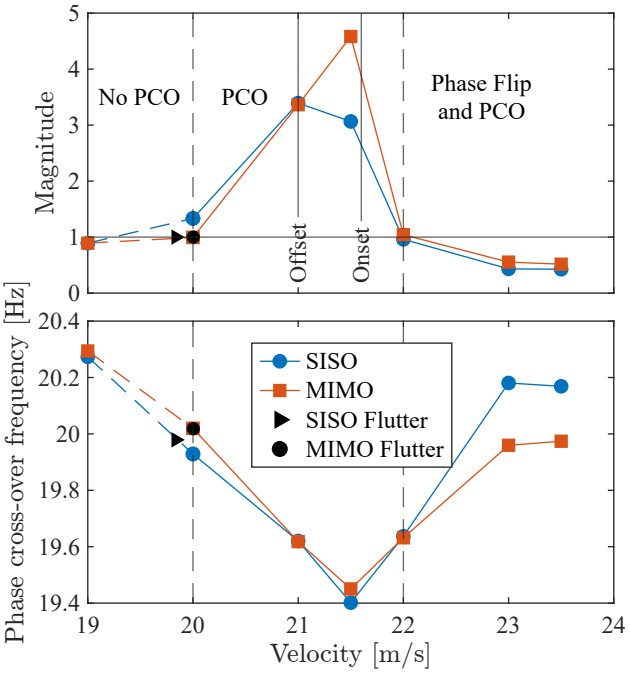

Fig. 22 Comparison SISO vs. MIMO $\alpha = 2°$

Another way to present the PFM results is given in Figure 25, which shows the amount of mass that needs to be added to the nominal configuration to reach the flutter boundary for the MIMO PFM results. This alternative way of representing the flutter margin is valid for both SISO and MIMO PFM. At the flutter boundary of the nominal system, the value for $\Delta p_f = 0$. For MIMO PFM, the value of Δp_f can be calculated using [11]

$$\Delta p_{f,i} = p_f - \frac{1}{\lambda\left(\omega_{\text{pco},i}\right)} \tag{19}$$

2. Flutter Modes

Using the measured accelerations during the direct flutter tests, and the FRFs measured during the PFM tests, the flutter modes as measured directly and through the MIMO PFM results can be compared. The comparison for the dynamic behaviour for $\alpha = 2°$ is shown in Figure 26 for phase angles 0°, 90°, 180° and 270°, with the dynamically deformed structure indicated with the black lines and markers with the dynamically undeformed structure being indicated with the light grey lines and markers.

Looking at the full dynamic motion of the flutter mode, both the direct flutter test, MIMO PFM and SISO PFM results show a similar flutter mode, with the second bending mode and first torsion mode being identifiable. When looking at the markers closest to the tip rod, which are located on the fourth and fifth line from the root, it can be seen that the second bending mode and first torsion mode show a phase difference, as the displacement seen by these markers is influenced by both second bending and first torsion in different amounts at the phases shown.

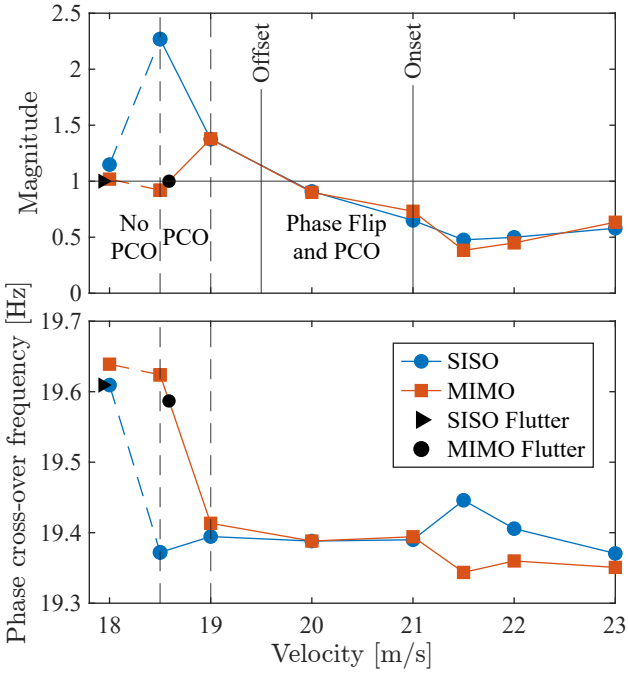

Fig. 23 Comparison SISO vs. MIMO α = 4°

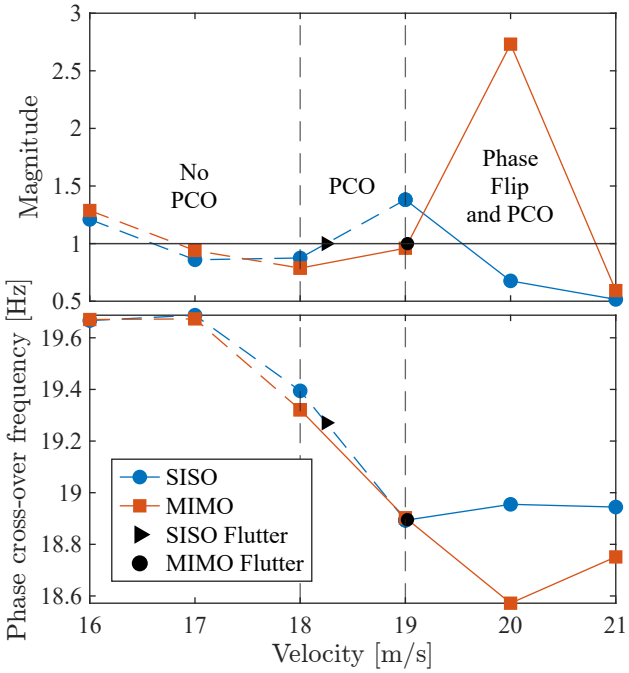

Fig. 24 Comparison SISO vs. MIMO α = 6°

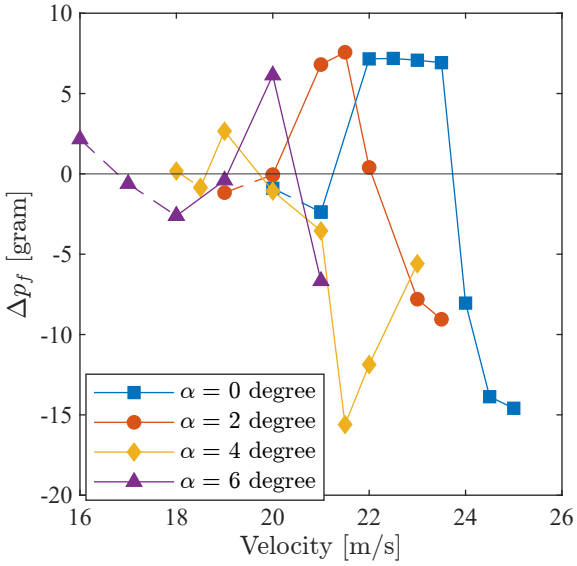

Fig. 25 Δp_f for all α's

Coming back to the full dynamic flutter mode, shown in Figure 26, it can be seen that the deformed shape at 0° and 180° phase shows the main motion of the wing to be in the opposite direction, which is true for both the MIMO and SISO PFM flutter modes. To be able to quantify the similarity of the flutter modes as identified using MIMO PFM, SISO PFM and direct flutter tests, the modal assurance criterion (MAC_{ODS}) value was calculated, with the acceleration measured at each accelerometer position being used as a DOF of each shape. For the comparison between the MIMO PFM flutter modes and the direct flutter test flutter modes, the calculated MAC_{ODS} value for $\alpha = 2°$ was 0.76, with the MAC_{ODS} values for $\alpha = 0°$ and 4° being equal to 0.78 and 0.75 respectively. For the comparison between the SISO PFM flutter modes and the direct flutter test flutter modes, the MAC_{ODS} value was 0.72, 0.78, 0.67 for $\alpha = 0°$, 2° and 4° respectively. The high MAC_{ODS} values of the dynamic flutter modes identified through MIMO and SISO PFM indicate

that they are in good agreement with the dynamic flutter mode measured during direct flutter testing.

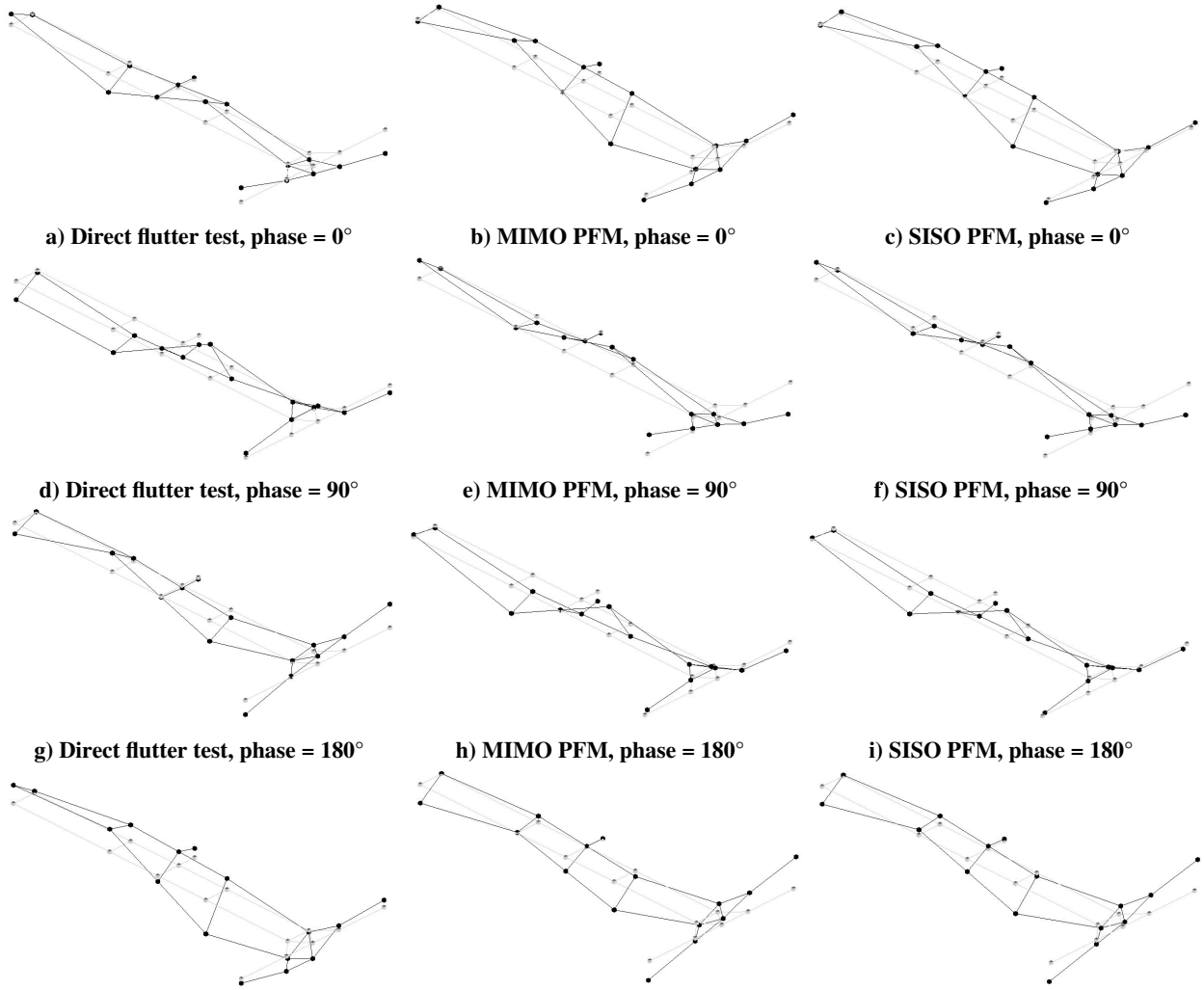

a) Direct flutter test, phase = 0° **b) MIMO PFM, phase = 0°** **c) SISO PFM, phase = 0°**

d) Direct flutter test, phase = 90° **e) MIMO PFM, phase = 90°** **f) SISO PFM, phase = 90°**

g) Direct flutter test, phase = 180° **h) MIMO PFM, phase = 180°** **i) SISO PFM, phase = 180°**

j) Direct flutter test, phase = 270° **k) MIMO PFM, phase = 270°** **l) SISO PFM, phase = 270°**

Fig. 26 Dynamic flutter mode shape comparison, $\alpha = 2°$, looking upstream

3. Eigenvectors

As the gain and phase cross-over frequencies are derived from the eigenvalues of the $[T(i\omega)]$ matrix given by equation (18), the corresponding eigenvectors may also be found. From an eigenvector, the relative gain and phase between the directions of motion of the mass can be determined. In the case of an undeformed wing, the coupled motion found using the eigenvector corresponding to λ_2 is dominated by the z-component, with the x-component being negligible. When the angle of attack is increased, the deflections experienced by the wing are increased, which results in an increased coupling because of the coupling between the in-plane motion and the torsional motion of the wing. The effect of increased coupling with increasing angle of attack at 20 m/s can be seen in Figure 27 for $\alpha = 0°, 2°$ and $4°$ respectively. Looking at the eigenvector for $\alpha = 0°$ it can be seen that the x-component is not equal to zero, as would be expected in this limit case, but has a maximum value of 0.2, and might have been caused by the slight wing bending caused in previous experiments, manufacturing imperfections or oscillating drag induced by the AOA oscillations.

Specifically looking at the coupling at or around the measured flutter boundary shown in Figure 28, it can be seen that the x-contribution for $\alpha = 0°$ remains around 0.2 independent of the velocity, which is as expected, as the wing is not deformed. Looking at the coupling for $\alpha = 2°$ and $4°$ a clear peak in the x-contribution can be seen and is found

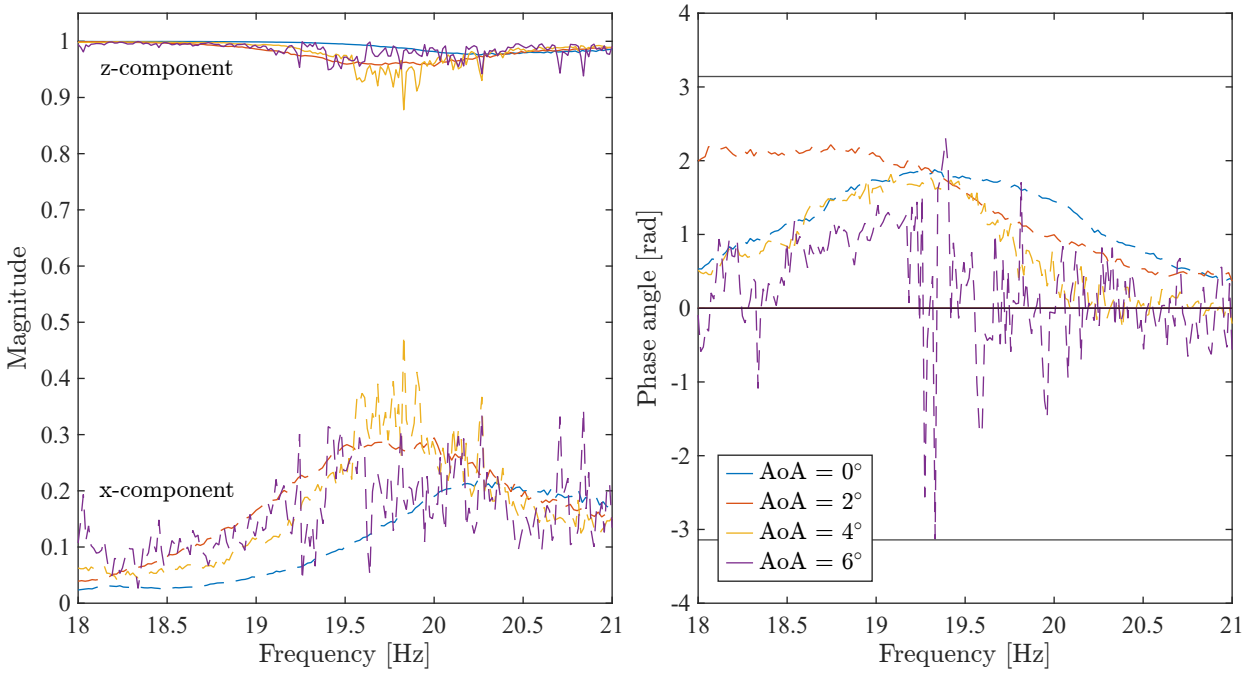

Fig. 27 Eigenvector at 20 m/s

close to the LCO frequency of the nominal system. The peak in x-contribution can be explained because when the 2nd Bending – 1st Torsion flutter mechanism is approached, the bending and torsion modes couple, resulting in an increased coupling in the z- and x-directions.

As stated previously in Section II.B, the eigenvector found from the $[T\,(i\omega)]$ matrix and corresponding to λ_2 shows the flutter mode at the location of the stabilising parameter based on the measured response. At the flutter velocity and frequency, the eigenvector shows the required response of the aeroelastic system to cancel the input and indicate the flutter boundary of the nominal system..

C. Comparison

Following the SISO and MIMO PFM results discussed above, a comparison between the SISO and MIMO PFM results, direct flutter results and numerical results can be presented. An overview of the different results is shown in Table 4, and it shows that the nominal flutter velocities of the MIMO and SISO PFM methods are up to 20 % lower than the direct flutter onset velocities, but only 4.8 % (MIMO) and 8.2 % lower than the direct flutter offset velocities. A visual presentation of the different velocities is shown in Figure 29, with the PFM results shown in this figure corresponding to the MIMO PFM results.

Looking at the PCO flutter frequencies, both the SISO and MIMO PFM results show differences of less than 0.9 % for $\alpha = 0°$, 3.2 % for $\alpha = 2°$ and 2 % for $\alpha = 4°$. Comparing the PCO flutter frequencies between the SISO and MIMO PFM results, a minimal difference is found for $\alpha = 0°$, which is increasing to 2 % for $\alpha = 6°$.

However, even with these differences, both the SISO and MIMO PFM exhibit a reduction in LCO frequency with increasing static deflections, as was found by Tang and Dowell [19].

The difference between the MIMO and SISO PFM results shown in Table 4 are caused by the addition of the effects in the x-direction to the MIMO solution, with the SISO PFM method providing good results with considerably less effort. However, the MIMO PFM results give a result that is closer to the directly measured flutter velocities because of the inclusion of the effects of the stabilising mass in the x-direction.

Looking further at Figure 29, it can be seen that the FEM model tuned to the GVTs, shows good agreement with the expected flutter onset velocities but also some differences that cause the numerically predicted flutter velocities to be higher than the measured onset velocities.

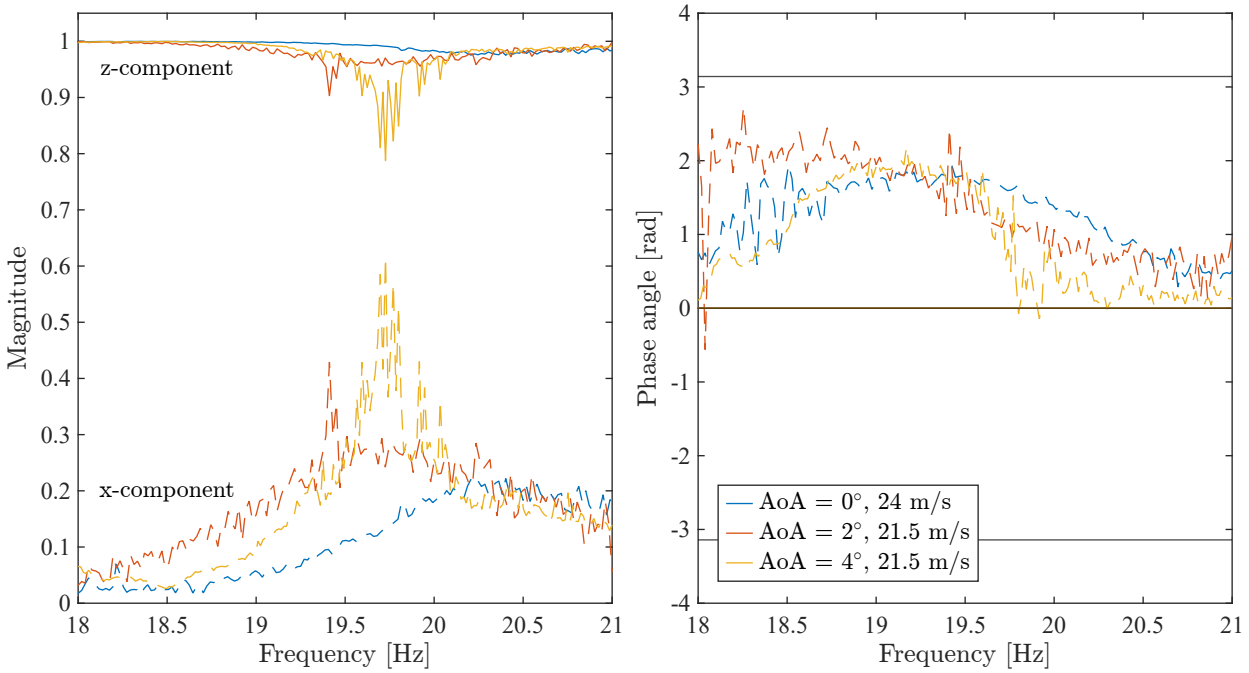

Fig. 28 Eigenvector at flutter onset

Table 4 Comparison Flutter Velocity

	Numerical	Direct			SISO			MIMO		
α (°)	(m/s)	Onset (m/s)	Offset (m/s)	ω_f (Hz)	V_f (m/s)	ω_{pco} (Hz)	MAC_{ODS}	V_f (m/s)	ω_{pco} (Hz)	MAC_{ODS}
0	25	24.2	21.5	20.3	21.0	20.42	0.72	21.1	20.48	0.78
2	24	21.6	21	19.4	19.8	19.98	0.78	20.0	20.02	0.76
4	22	21	19.5	19.2	17.9	19.64	0.67	18.6	19.59	0.75
6	21	> 29	> 29	-	18.2	19.27	-	19.0	18.89	-

D. Effect of Shaker Excitation

Combing back to the under-identification of the flutter velocity, it is assumed that because of the large vibrations seen during the direct flutter tests, the wing experiences subcritical Hopf-bifurcation and the occurrence of a fold point that is similar to the behaviour observed by Tang and Dowell [19–21] on highly flexible wings. Hence, the shaker excitation level during the PFM tests cause flutter to start at lower velocities.

To determine the effect of the shaker excitation force on the flutter margin, the input voltage was lowered from 0.4 V (Gain 1) to 0.2 V (Gain 2) and the FRFs were obtained for a range of velocities between 22 m/s and 24 m/s at $\alpha = 0°$. Looking at Figures 30 and 31 for 22 m/s and 23 m/s respectively, both the magnitude and phase are influenced by the excitation force. However, when the wing approaches the flutter onset velocity, as shown in Figure 32, the difference in FRF behaviour due to different excitation amplitudes becomes negligible.

The presented results suggest that a larger excitation force results in a higher gain amplitude at the cross-over frequency and a higher phase cross-over frequency. However, when the wing approaches the linear flutter onset velocity, the effect of the excitation amplitude becomes small.

Because of the low number of sample points and the shaker design, several uncertainties with respect to the shaker excitation level exist. Therefore, to be able to fully understand the effect of excitation level on the predicted flutter velocity, further investigation into the property of the flutter pod is required. For example, due to the design of the shaker, its performance as a function of excitation levels should be investigated in more detail first. In addition, the

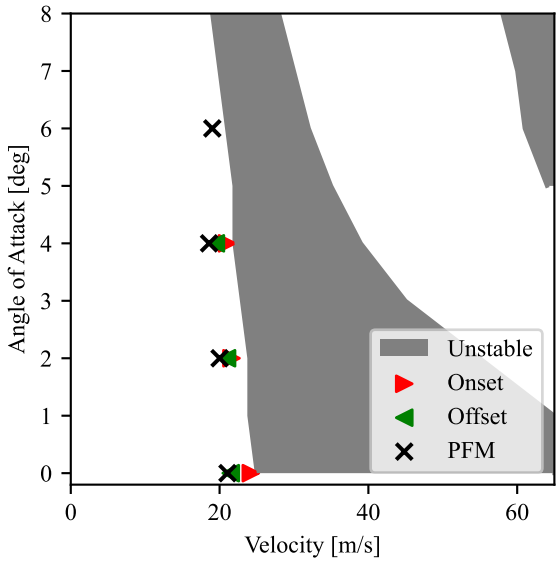

Fig. 29 Comparison between numerical, direct flutter test and MIMO PFM results

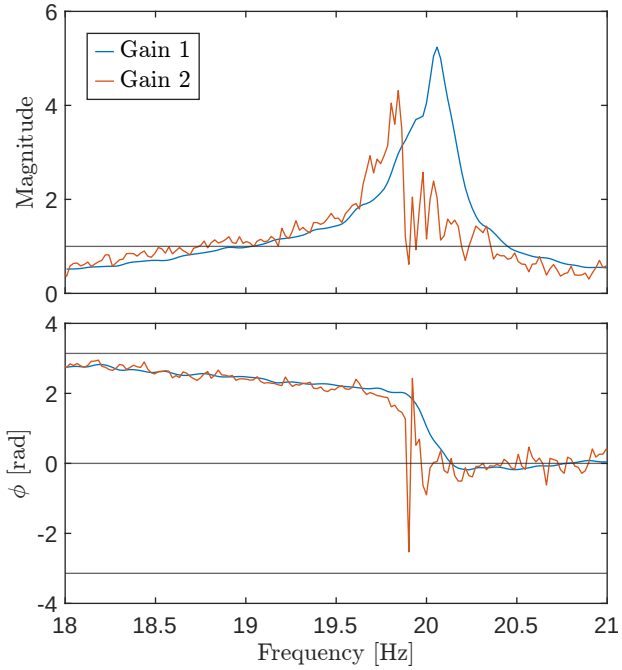

Fig. 30 SISO z-response to z-excitation with lower shaker excitation V = 22 m/s

measurements should be repeated at more free-stream velocities and angles of attack.

VII. Conclusions and Outlook

The presented research shows a successful application of the MIMO PFM method to a highly flexible wing under large initial deflections to positively identify the flutter velocity of the aeroelastic system. With the addition of the stabilising mass at the mid-span position at the leading edge, the flutter velocity of the nominal system has been safely identified without the use of a numerical model, with the numerical model only being used to design the experiment,

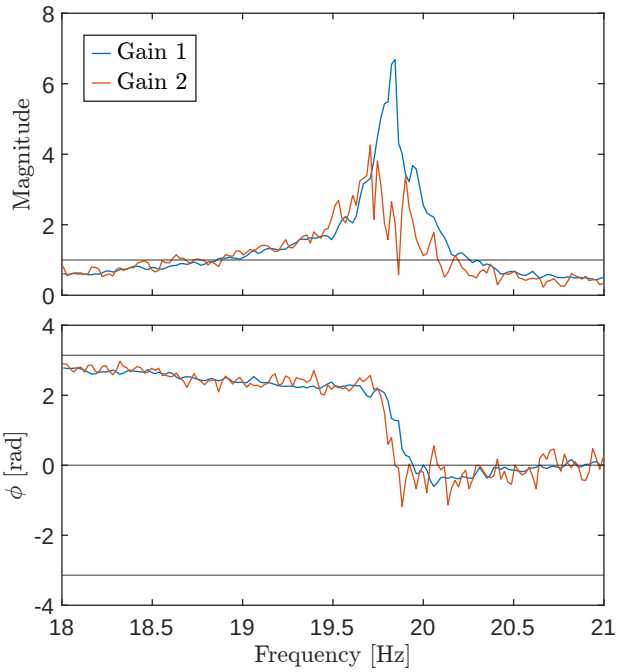

Fig. 31 SISO z-response to z-excitation with lower shaker excitation V = 23 m/s

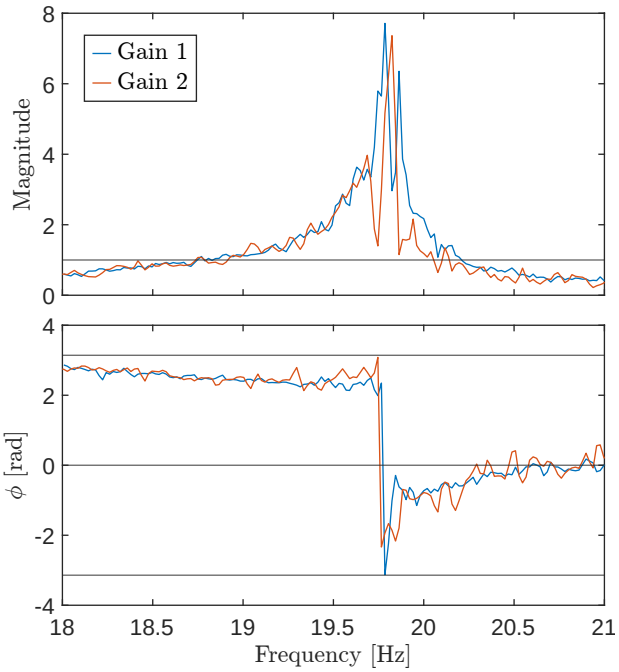

Fig. 32 SISO z-response to z-excitation with lower shaker excitation V = 24 m/s

which shows the potential of the PFM method for performing safer, shorter and consequently cheaper flight tests for the certification procedure of new aircraft configurations.

The experimental results provided three types of signals, which are a signal without a phase cross-over (PCO), a signal with a PCO and a signal with a phase flip (where the signal jumps from $+\pi$ to $-\pi$ or vice versa) and PCO on the real positive axis. The PCO frequency and the corresponding gain indicate the flutter margin and frequency of the aeroelastic system.

Following the flutter margins, both the SISO and MIMO PFM results under-identified the flutter onset velocity by up to 20 %, with the offset velocities being under-identified by a maximum of 8.2 % (SISO) and 4.8 % (MIMO). The differences in identified flutter velocity using MIMO and SISO PFM are increasing with angle of attack, α, with a maximum difference of 4.4 % reached for $\alpha = 6°$. Comparing the PCO flutter frequency, the difference between the SISO and MIMO PFM methods is also increasing with increasing α and reaches a maximum of 2 %, with a maximum difference of 3.2 % found between the PFM and direct tests. Going further into the measured responses, the flutter shapes as identified using MIMO PFM showed good agreement with the directly measured flutter shape, as the MAC value was greater than 0.75 for all angles of attack.

Even though the MIMO and SISO PFM results show differences between their results, both methods identify a reducing flutter velocity and frequency, which is in line with the direct flutter test performed during the wind tunnel campaign. However, within the range of deflections experienced during the test campaign, it can be concluded, that the SISO PFM method was able to identify the flutter offset velocity at slightly higher errors than those of MIMO PFM, but with considerably less effort.

On top of the MIMO and SISO PFM measurements, a set of SISO PFM measurements was performed using a lowered shaker excitation level to determine the effect of the shaker excitation on the wing, as it was suspected the wing experienced subcritical Hopf-bifurcation and fold points similar to the behaviour seen on very flexible wings by Tang and Dowell [20]. The measurement series showed an influenced FRF behaviour at velocities below the flutter onset velocity, with the influenced FRF behaviour disappearing close to this velocity, with further measurements being required to fully understand the effect of the shaker excitation level.

Future work relating to the PFM method will be focused on signal processing and data analysis. Aspects that need to be investigated are the possible relaxation of the phase cross-over and the effect of the phase flip which causes the loss of the phase cross-over. Furthermore, the post-flutter effects on the eigenvalues and eigenvectors used during the

analysis need to be investigated, with further investigation of the effects of different levels of excitation on the measured FRFs also needing to be performed.

Furthermore, the nominal MIMO-PFM flutter velocities were closer than the SISO results to the directly obtained flutter velocities, but not very significantly. A reason is that the added mass was located at a mid-span location, where the static deflections are much smaller than at the wing's tip. Therefore, further tests should be performed with masses at places where the different directions are similarly important, such as the wing's tip or under-wing external stores.

VIII. Data Archive

The experimental data that is presented in this paper will be made available in a data archive of the 4TU.ResearchData center that can be found under the DOI: `https://doi.org/10.4121/21656672`

References

[1] European Union Aviation Safety Agency, "Certification Specifications and Acceptable Means of Compliance for Large Aeroplanes (CS-25) Amendment 27," , Nov. 2021. URL `https://www.easa.europa.eu/downloads/134259/en`.

[2] Federal Aviation Administration, "AC 23.629-1B - Means of Compliance with Title 14 CFR, Part 23, § 23.629, Flutter," , Sep. 2004.

[3] Hodges, D. H., and Pierce, G. A., Introduction to structural dynamics and aeroelasticity, 2nd ed., No. 15 in Cambridge aerospace series, Cambridge University Press, New York, 2011. URL `https://doi.org/10.1017/CBO9780511997112`.

[4] Zimmerman, N. H., and Weissenburger, J. T., "Prediction of flutter onset speed based on flight testing at subcritical speeds," Journal of Aircraft, Vol. 1, No. 4, 1964, pp. 190–202. https://doi.org/10.2514/3.43581, URL https://arc.aiaa.org/doi/10.2514/3.43581, publisher: American Institute of Aeronautics and Astronautics.

[5] Dimitriadis, G., and Cooper, J. E., "Flutter Prediction from Flight Flutter Test Data," Journal of Aircraft, Vol. 38, No. 2, 2001, pp. 355–367. https://doi.org/10.2514/2.2770, URL https://arc.aiaa.org/doi/10.2514/2.2770.

[6] Cooper, J. E., Emmett, P. R., Wright, J. R., and Schofield, M. J., "Envelope function - A tool for analyzing flutter data," Journal of Aircraft, Vol. Vol. 30, No. No. 5, 1993, pp. 785–790. https://doi.org/10.2514/3.46412, URL https://arc.aiaa.org/doi/pdf/10.2514/3.46412.

[7] Raveh, D. E., Iovnovich, M., and Nahom, T., "Wind-Tunnel Study of the ARMA Flutter Prediction Method," 2018 AIAA/ASCE/AHS/ASC Structures, Structural Dynamics, and Materials Conference, American Institute of Aeronautics and Astronautics, Kissimmee, Florida, 2018. https://doi.org/10.2514/6.2018-0702, URL https://arc.aiaa.org/doi/10.2514/6.2018-0702.

[8] Sodja, J., Roizner, F., De Breuker, R., and Karpel, M., "Experimental characterisation of flutter and divergence of 2D wing section with stabilised response," Aerospace Science and Technology, Vol. 78, 2018, pp. 542–552. https://doi.org/10.1016/j.ast.2018.05.014, URL https://www.sciencedirect.com/science/article/pii/S1270963818305868.

[9] Roizner, F., and Karpel, M., "Linear and Nonlinear Flutter Analyses Using Dynamic Response Computations," 58th AIAA/ASCE/AHS/ASC Structures, Structural Dynamics, and Materials Conference, AIAA SciTech Forum, American Institute of Aeronautics and Astronautics, 2017. https://doi.org/10.2514/6.2017-1594, URL https://arc.aiaa.org/doi/10.2514/6.2017-1594.

[10] Roizner, F., and Karpel, M., "Parametric Flutter Margin Method for Aeroservoelastic Stability Analysis," AIAA Journal, Vol. 56, No. 3, 2018, pp. 1011–1022. https://doi.org/10.2514/1.J056514, URL https://arc.aiaa.org/doi/10.2514/1.J056514.

[11] Roizner, F., and Karpel, M., "Sensitivity of Aeroservoelastic Stability Characteristics Using Parametric Flutter Margins," Journal of Aircraft, Vol. 56, No. 4, 2019, pp. 1387–1397. https://doi.org/10.2514/1.C035286, URL https://arc.aiaa.org/doi/10.2514/1.C035286.

[12] Roizner, F., Raveh, D. E., and Karpel, M., "Safe Flutter Tests Using Parametric Flutter Margins," Journal of Aircraft, Vol. 56, No. 1, 2019, pp. 228–238. https://doi.org/10.2514/1.C035045, URL https://arc.aiaa.org/doi/10.2514/1.C035045.

[13] Karpel, M., McCrink, M., Heidersbach, R., and Seth, D., "Safe Wind Tunnel Flutter Test Using a Shaker and Mass Margins," International Forum on Aeroelasticity and Structural Dynamics, Madrid, Spain, 2022.

[14] Karpel, M., "Unified Framework for Aeroservoelastic Response and Stability Analysis, Design and Testing," International Forum on Aeroelasticity and Structural Dynamics, Savannah, Georgia, USA, 2019.

[15] Howcroft, C., Calderon, D., Lambert, L., Castellani, M., Cooper, J. E., Lowenberg, M. H., and Neild, S., "Aeroelastic Modelling of Highly Flexible Wings," 15th Dynamics Specialists Conference, AIAA SciTech Forum, American Institute of Aeronautics and Astronautics, 2016. https://doi.org/10.2514/6.2016-1798, URL https://arc.aiaa.org/doi/10.2514/6.2016-1798.

[16] Mertens, C., Sodja, J., Sciacchitano, A., and van Oudheusden, B., "Experimental Aeroelastic Characterization of a Very Flexible Wing in Steady and Unsteady Inflow," AIAA SCITECH 2022 Forum, American Institute of Aeronautics and Astronautics, San Diego, CA & Virtual, 2022. https://doi.org/10.2514/6.2022-1344, URL https://arc.aiaa.org/doi/10.2514/6.2022-1344.

[17] Avin, O., Raveh, D. E., Drachinsky, A., Ben-Shmuel, Y., and Tur, M., "Experimental Aeroelastic Benchmark of a Very Flexible Wing," AIAA Journal, Vol. 60, No. 3, 2022, pp. 1745–1768. https://doi.org/10.2514/1.J060621, URL https://arc.aiaa.org/doi/10.2514/1.J060621, publisher: American Institute of Aeronautics and Astronautics.

[18] Drachinsky, A., Avin, O., Raveh, D. E., Ben-Shmuel, Y., and Tur, M., "Flutter Tests of the Pazy Wing," AIAA Journal, Vol. 60, No. 9, 2022, pp. 5414–5421. https://doi.org/10.2514/1.J061717, URL https://arc.aiaa.org/doi/10.2514/1.J061717, publisher: American Institute of Aeronautics and Astronautics.

[19] Tang, D. M., and Dowell, E. H., "Effects of geometric structural nonlinearity on flutter and limit cycle oscillations of high-aspect-ratio wings," Journal of Fluids and Structures, Vol. 19, No. 3, 2004, pp. 291–306. https://doi.org/10.1016/j.jfluidstructs.2003.10.007, URL https://www.sciencedirect.com/science/article/pii/S0889974604000106.

[20] Tang, D., and Dowell, E. H., "Experimental and Theoretical Study on Aeroelastic Response of High-Aspect-Ratio Wings," AIAA Journal, Vol. 39, No. 8, 2001, pp. 1430–1441. https://doi.org/10.2514/2.1484, URL https://arc.aiaa.org/doi/10.2514/2.1484.

[21] Tang, D., and Dowell, E. H., "Limit-Cycle Hysteresis Response for a High-Aspect-Ratio Wing Model," Journal of Aircraft, Vol. 39, No. 5, 2002, pp. 885–888. https://doi.org/10.2514/2.3009, URL https://arc.aiaa.org/doi/10.2514/2.3009.